Revising the Rainfall Anomaly Index for Extreme Rainfall Variability Analysis

Kenneth Ekpetere[1*]

[1] CAPA Strategies, Portland, Oregon, USA, 97242.

*Corresponding author: Dr. Kenneth Ekpetere (Kenneth.ekpetere@gmail.com)

Current Address: CAPA Strategies, P.O Box 42223, Portland, Oregon, USA, 97242-0203.

Email-addresses: kenneth.ekpetere@gmail.com (K. Ekpetere).

Highlights:

- Two indices – MRAI and SRAI are proposed for estimating extreme rainfall anomaly.
- Proposed indices demonstrates strong agreement with RAI index model.
- MRAI and SRAI captures extremely wet dry anomaly conditions in CONUS.
- IMERG showed prospects for modeling the MRAI/SRAI indices.

Abstract

This research proposes two revised rainfall anomaly index models – the Modified Rainfall Anomaly Index (MRAI) and the Standardized Rainfall Anomaly Index (SRAI). The proposed models addresses concerns with the existing Rainfall Anomaly Index (RAI) model, such as the RAI's inability to capture extremely dry and extremely wet ranges of rainfall anomaly efficiently, and the crude rationale behind the RAI formulation. To assess the models' performance on a continental scale, the Integrated Multi-Satellite Retrievals for GPM (IMERG) was adapted for locations in Conterminous United States (CONUS). The IMERG data provides an opportunity to scale the study to ungaged locations and beyond the CONUS. To enhance the robustness of the analysis and increase confidence in model outputs, daily annual maximum series (AMS) from 2,360 stations provided by the National Oceanic Atmospheric Administration (NOAA) served as reference data. The station data was applied to the existing RAI model, and IMERG applied to proposed MRAI and SRAI indices. Based on the study findings, the kurtosis of the MRAI index ranged from 0 to +0.9 and was consistently higher than SRAI and RAI across the years. The SRAI exhibited a kurtosis range between -0.9 and -0.1. The median index range of SRAI lies between -2 and 0, MRAI lies between 0 and +2, while RAI lies between -1 and +1. Comparing the proposed MRAI and reference RAI, the statistics showed an average PRB of -23.5, RMSE of 0.93, MBR of 0.74, NSE of 0.82, and KGE of 0.53. In contrast, the statistics between the SRAI and RAI indices recorded an average PRB of -14.5, RMSE of 1.7, MBR of 0.8, NSE of 0.41, and KGE of 0.46, respectively. Spatially, the MRAI exhibited a tendency to capture positive rainfall anomalies leaning towards extremely wet conditions, while the SRAI demonstrated a tendency to capture negative rainfall anomalies leaning towards extremely dry conditions. Together, the three indices shows prospects for climate change study applications especially when used together.

1 Introduction

Rainfall indices for measuring anomalies from extreme rainfall events (severe rainfall and droughts) have become vital tools for climate change studies worldwide (K. O. Ekpetere et al., 2024; Raziei, 2021; Vicente-Serrano et al., 2010). With increasing global fluctuations in droughts and floods (Gil-Alana et al., 2022; Huang et al., 2021), scientists are tasked with identifying indices that best capture these extreme variations. Due to global fluctuations in precipitation, arid regions are becoming drier while flood-prone areas are experiencing intensified flooding driven by climate change (Armal & Khanbilvardi, 2019; Córdova et al., 2022). Although the Intergovernmental Panel on Climate Change (IPCC) has reported a shift towards wetter conditions on a global scale as a result of climate change, regional trends deviate substantially (Armal & Khanbilvardi, 2019; Baratto et al., 2024; Xu et al., 2022; L. Yu et al., 2016).

Over the years, several indices have been developed for drought monitoring, including the Standardized Precipitation Index (SPI) (Mckee et al., 1993), the Standardized Evapotranspiration Index (SPEI) (Vicente-Serrano et al., 2010), the Palmer Drought Severity Index (PDSI) (Palmer, 2006), and the decile index, which are used globally (Raziei, 2021). These indices are straightforward, requiring only precipitation as input, and have proven effective in studies on extreme droughts worldwide (Gavahi et al., 2022; Kumar et al., 2022; G. Zhang et al., 2021). On the other hand, the Rainfall Anomaly Index (RAI), developed by Van Rooy in 1965 (Van-Rooy, 1965), has remained a standard for calculating anomalies aimed at assessing extreme rainfall changes globally (Costa & Rodrigues, 2017; Koudahe et al., 2017; Van-Rooy, 1965). However, RAI has shortcomings that have been overlooked over the years (Raziei, 2021), particularly in its use of an arbitrary ranking system to select values for the model.

The RAI model uses a ranking system to assign magnitudes to negative and positive precipitation anomalies (K. O. Ekpetere et al., 2024; Raziei, 2021; Van-Rooy, 1965). Though straightforward, relying on a simpler normalization process than SPI, the rationale behind the ranking magnitude has been questioned (K. O. Ekpetere et al., 2024; Nasta et al., 2020; Raziei, 2021; S. Wang et al., 2019). According to RAI's formula, positive anomalies use the average of the 10 highest recorded precipitation values, while negative anomalies use the average of the 10 lowest values after ranking (Van-Rooy, 1965). The choice of 10 is arbitrary, with Van Rooy selecting this number based on the conception that averaging the 10 extremes would represent mean conditions of an extreme dry or wet year (K. O. Ekpetere et al., 2024; Raziei, 2021). However, climatologically, a 10-year timeframe is insufficient for climate change measurement, where a 30+ year period is considered standard (Corringham et al., 2022; Ripple et al., 2024). RAI formulation is further limited when data length is short (WMO, 2009). To address these issues, this study proposes two Rainfall Anomaly indices that incorporate the complete range of rainfall data for RAI model formulation.

Another contribution of this study is leveraging the Integrated Multi-Satellite Retrievals for Global Precipitation Measurement (IMERG), a satellite precipitation product (SPP) that can extend rainfall anomaly calculations from to global scale, and covering data-scarce locations (Aksu et al., 2023; Huffman, 2020; Ning et al., 2017; Pucknell et al., 2020). Earlier studies on anomaly indices primarily relied on rainfall records from point-location stations (Lau & Behrangi, 2022) or watersheds (Noor et al., 2021), and these station records are particularly limited in ungaged areas (Bonnin et al., 2006; K. Ekpetere, 2024). This scarcity can introduce uncertainty in the validity and reliability of such applications (Alamri & Subyani, 2017; Costa & Rodrigues, 2017; De Paola et al., 2014; Duque-Gardeazabal & Rodríguez, 2023; D.-E. Kim et al., 2019; Noor et al., 2021; Tan & Yang, 2020; Willems, 1999, 2000). To fill these gaps, SPPs like IMERG are essential for supplementing missing

gage data globally (K. Ekpetere, 2024; K. Ekpetere et al., 2023; NOAA-OWP, 2022; Perica et al., 2013), offering broad precipitation coverage (J. Chen et al., 2022; H. Gu et al., 2016; Pradhan et al., 2022; Schamm et al., 2014; G. Zhao et al., 2022), and ensuring reliable precipitation availability (Kasi et al., 2022; D.-E. Kim et al., 2019; Mab et al., 2019; Tan & Yang, 2020).

Previous research has shown that IMERG aligns well with station observations (Anjum et al., 2018; Dehaghani et al., 2023; K. O. Ekpetere & Coll, 2024; Huffman, 2020; Min Yang et al., 2019; J. Wang et al., 2021; Y. Wang et al., 2023; Weng et al., 2023; Yuan et al., 2018; H. Zhao et al., 2018; Zhou et al., 2023). IMERG provides global coverage from 0 – 65° N/S, with a spatial resolution of 0.1° and a temporal resolution of half-hour (Huffman, 2020; Peinó et al., 2023; Sathianarayanan & Hsu, 2023; Tang et al., 2020; Xin et al., 2022). IMERG's advanced hydrological applications arise from its integration of optical and radar sensor data. It combines outputs from the Global Precipitation Measurement (GPM) and Tropical Rainfall Measuring Mission (TRMM) and is calibrated with over 80,000 Global Precipitation Climate Center (GPCC) gage records (Anjum et al., 2018; Huffman, 2020; Schamm et al., 2014). IMERG estimates have proven invaluable for flood risk assessment and management globally, aiding in planning flood control infrastructure such as dams, culverts, levees, and bridges, which protect farmlands, buildings, and lives (Adeel et al., 2023; Ahn et al., 2014; Bathrellos et al., 2016; Corringham et al., 2022; Devitt et al., 2021; Gabriels et al., 2022; Quinn et al., 2019).

Numerous studies have sought to improve the RAI index, either by revising the RAI model (Raziei, 2021) or evaluating the strengths and weaknesses of the current RAI model (K. O. Ekpetere et al., 2024). Raziei (2021) proposed a new RAI index that utilizes the 5th and 95th percentiles of ranked precipitation data, averaging the bottom 5% and top 5% of data rather than averaging the bottom and top 10 data records, as proposed by Van Rooy in 1965. Raziei's revised RAI index has

shown promise but was found to be more applicable to arid regions with a high probability of zero precipitation (PZP). The use of only 45 gauging stations for Iran also introduced considerable uncertainty in the index model validity proposed by Raziei (2021). In a related study, Armal & Khanbilvardi (2019) examined temporal anomalies in extreme U.S. precipitation and climate influences using quartile perturbations across 1,041 stations, noting drier conditions in mid-20th century and wetter conditions in recent decades (Armal & Khanbilvardi, 2019). Nasta et al. (2020) analyzed seasonal-rainfall anomalies' impact on water balance components using the SWAT model in southern Italy, identifying seasonal-dependent regression equations linking water yield and dryness index during the wet season (Nasta et al., 2020). Additionally, Henny et al. (2023) used Global Historical Climate Network (GHCN) data to examine extreme U.S. precipitation between 1979 and 2019 (Henny et al., 2023). Le et al. (2023) highlighted climate-driven predictions of seasonal precipitation through seasonal sea surface temperature (Le et al., 2023). Other studies have explored large-scale circulation anomalies' role in U.S. extreme precipitation changes (Yu et al., 2016), the North American Monsoon Systems' (NAMS) multi-decadal variability from 1948 to 2009 (Arias et al., 2012), and the primary climatic factors influencing precipitation anomalies in South America such as intensity, the El Niño effect, and meridional position (Córdova et al., 2022).

While prior research has examined the strengths and limitations of the current RAI index, limited efforts have been made to develop a model that fully leverages the available rainfall records for optimal anomaly representation (Da Silva et al., 2021; Peinó et al., 2023; Raziei, 2021; Tan & Santo, 2018; Yuan et al., 2018). To address this gap, this study proposes two revised RAI models: (1) the Modified Rainfall Anomaly Index (MRAI), which incorporates the entire data range by factoring in the minimum and maximum values in the series, and (2) the Standardized Rainfall Anomaly Index (SRAI), which considers the standard deviation of extreme rainfall events. MRAI thus reflects

anomalies relative to the full data span, while SRAI highlights deviations based on average and extreme conditions.

The objectives of this study are: (1) to revise the existing RAI index by proposing the MRAI and SRAI as alternative models to address known RAI uncertainties, (2) to examine the potential and limitations of IMERG data for computing anomaly indices across various stations in CONUS, and (3) to perform a comparative assessment of the proposed rainfall anomaly indices (MRAI and SRAI) across the 2,360 stations—evaluating these indices on yearly, regional, and full-scale levels. The remainder of this paper is organized as follows: Section 2 describes the study area and data, Section 3 details the methodology, Section 4 presents and discusses the results, and Section 5 offers conclusions.

2 Study Area and Data

2.1 *Study Area*

The 2,360 stations used in this study are located within CONUS, covering an estimated area of 3,119,885 square miles (approximately 8,080,464 km²), with roughly 83.65% of this area comprising land. Mean annual precipitation in CONUS varies significantly from as little as 2.5 inches in the driest regions (e.g., Nevada and Arizona) to over 200 inches in the eastern and southern areas (e.g., Louisianna), generally following a west-to-east gradient (Figure 1). The selected NOAA stations corresponds to 2,360 unique pixels of IMERG data. At the time of this study, NOAA station data were unavailable for the northwestern part of CONUS, as coverage extensions were underway (NOAA, 2017, 2021; NOAA et al., 2015; NWS, 2020)

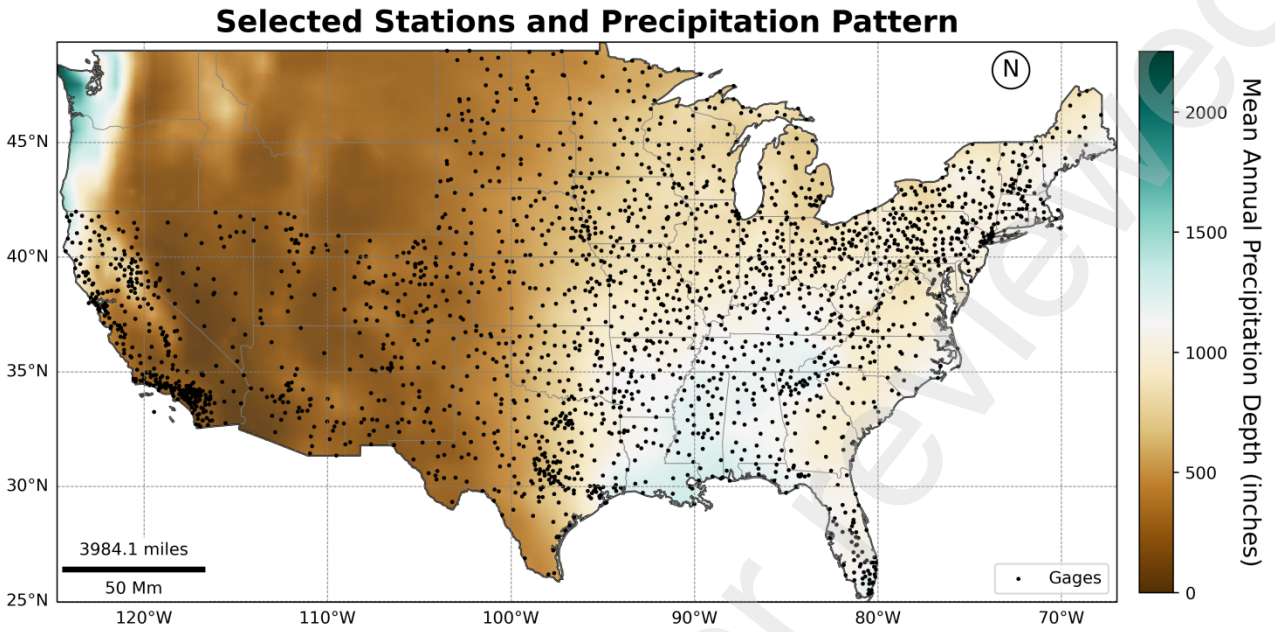

Figure 1. Extent of the conterminous United States (CONUS) highlighting the 2,360 NOAA stations and the mean annual precipitation depth (in inches). It is important to note that the Northwestern CONUS, which includes Idaho, Montana, Oregon, Washington, and Wyoming, does not have available station data at the time of this study.

2.2 *IMERG Precipitation Data*

IMERG data have a temporal resolution of half-hourly, a spatial resolution of 0.1° × 0.1°, and a coverage range of 0–65° N/S. The IMERG remote sensing precipitation data combine inputs from several algorithms: the Global Precipitation Measurement Profiling Algorithm (GPROF), the Precipitation Retrievals and Profiling Scheme (PRPS), the PERSIANN Cloud Classification System (PERSIANN-CCS), the Global Precipitation Climatology Project – monthly satellite-gage (GPCP-SG), and the Combined Radar Radiometer Algorithm (CORRA) (Huffman, 2020; Huffman et al., 2007). IMERG offers three distinct products: “Early-run”, “Late-run”, and “Final-run”.

The algorithm generates these products in stages. First, the “Early-run” estimates are produced, becoming available approximately 3.5 hours after observation time (AOT). Next, the “Late-run” estimates are released around 12 hours AOT. Finally, the “Final-run” estimates are produced about

three months AOT, following calibration by the Global Precipitation Climate Center (GPCC) (Dekai Lu & Bin Yong, 2018; Zhou et al., 2023). The IMERG Early and Late-run products incorporate climatological data for corrections, while the Final-run is calibrated using over 80,000 GPCC station observations worldwide (Gebregiorgis et al., 2018; Huffman et al., 2007; Pradhan et al., 2022; Schamm et al., 2014). The IMERG-Final product Version 07 was used in this study. The IMERG dataset spans from 2000 to the present (Huffman, 2020).

2.3 *NOAA Station Data*

The NOAA station dataset is the authoritative Annual Maximum Series (AMS) observation dataset, highly recommended for meeting national standards (Gao et al., 2018; Perica et al., 2013). The NOAA database provides the reference precipitation data for this study (NOAA, 2017). The AMS observations cover durations ranging from 5–minutes up to 60–days. The database includes records dating back to the 1950s (NOAA-OWP, 2022; Perica et al., 2013) and contains data from over 16,000 stations across CONUS. However, only about 2,360 stations meet the 22-year record requirement (2001–2022) and were used to validate the revised RAI indices (MRAI and SRAI). Table 1 compares the NOAA station data with the satellite-based IMERG data.

Table 1: Comparison of NOAA station data and IMERG satellite precipitation data.

Characteristics	NOAA station Data	IMERG Satellite Data
Spatial Resolution	≥ 200 m (varies)	0.1˚ (~11 km)
Temporal Resolution	5-min to 60-days	Half-hourly
Period	2001 – 2022	2001 – 2022
Sensor(s)	Rain gages	GMI & DPR
Area coverage	CONUS	Global

Calibration	Gage	TRMM, TMPA, & GPCC
Ownership	NOAA	NASA & JAXA
Reference	(Perica et al., 2011)	(Huffman et al., 2020)

3 Methods

3.1 *Calculating Annual Maximum Series (AMS) from IMERG*

The station-based AMS for NOAA data are precomputed and downloaded as-is (Bonnin et al., 2006; Perica et al., 2013). In contrast, IMERG data is available in 30-minute increments (Da Silva et al., 2021; Tang et al., 2020). To compute the daily annual maximums for each grid location, 48 overlapping 30-minute rainfall pixels were summed to create a 24-hour duration total. This accumulation period spans from January 1 at 00:00 UTC to December 31 at 23:30 UTC for each year. The data covers the years 2000 to 2023, though 2000 and 2023 were excluded due to incomplete records. For 2000, IMERG data begins only from June 3, while data from 2023 was excluded to align with the station record period. The accumulated daily annual maximum for each year (2001 to 2022) was calculated across all 2,360 IMERG pixels co-located with 2,360 stations (point-to-grid comparison).

3.2 *Computing RAI*

The RAI, developed by Van Rooy in 1965, is a rank-based system for measuring drought anomaly indices, assigning magnitudes to negative (deficit) and positive (surplus) precipitation anomalies (Van Rooy, 1965). This index helps classify rainfall anomalies by scaling extremes within a nine-category scheme, ranging from extremely wet (RAI $\geq$ 3) to extremely dry (RAI $\leq$ -3). Previous studies have demonstrated the classification scheme's applicability to various drought and excess

rainfall conditions, including flash droughts, meteorological drought, deep soil moisture drought, and hydrological drought (Raziei, 2021). The RAI is computed as shown in Equation 1 below.

$$RAI = \begin{cases} 3\left(\frac{P_n - \overline{P}}{\overline{M} - \overline{P}}\right) & \text{if } P > \overline{P}, \\ -3\left(\frac{P_n - \overline{P}}{\overline{L} - \overline{P}}\right) & \text{if } P < \overline{P} \end{cases} \quad (1)$$

In Equation 1, P_n represents the sequence of daily maximums for each year *n* (2001 to 2022), $\overline{P}$ is the mean precipitation for the series of daily maximums across all *n*, $\overline{M}$ is the average of the top 10 largest values from the *n* series, $\overline{L}$ is the average of the top 10 lowest values from the *n* series. The ± 3 is the standardization prefix is used to limit the lower and upper bounds of the anomalies to a unity-based feature scaling, ensuring that the anomalies are asymmetrically distributed between the predefined limits (-3 and +3). From Eq. (1), for a positive anomaly where $P_n - \overline{P}$ is less than 0, the prefix is assigned a negative value; conversely, where $P_n - \overline{P}$ is greater than 0, the prefix is assigned a positive value.

Equation 1 presents several uncertainties, such as the choice of the 10 smallest and 10 largest values in the AMS for computation, which is not scientifically justified. Additionally, the RAI has demonstrated strong performance in dry and moderate climates but has shown bias in highly humid regions, such as CONUS (Raziei, 2021). Raziei (2021) noted that the calculation of the top and bottom averages in Eq. (1) may skew the anomalies, warranting a revision to capture the full data range.

Table 2: Classification scheme of the RAI index (Raziei, 2021; Van Rooy, 1965).

RAI	Class description
≥ 3.00	Extremely wet
2.00 to 2.99	Very wet
1.00 to 1.99	Moderately wet
0.50 to 0.99	Slightly wet
-0.49 to 0.49	Near normal
-0.99 to -0.50	Slightly dry
-1.99 to -1.00	Moderately dry
-2.99 to -2.00	Very dry
≤ -3.00	Extremely dry

3.3 *Computing Modified Rainfall Anomaly Index (MRAI)*

The choice of 10 measurements from the series of AMS (n) for calculating $\overline{M}$ and $\overline{L}$ was arbitrarily made by Van Rooy in 1965, as he believed that the average of 10 extremes might represent the average conditions of an extremely wet and extremely dry year. Consequently, the RAI carries some uncertainties when there are fewer years of extremely dry and extremely wet rainfall derived from a complete dataset of no more than 10 years of AMS. To address this concern, the Modified RAI (MRAI) is proposed to fully accommodate the entire data range (i.e., the minimum and maximum values in the series). The MRAI provides an absolute measure of anomaly over a broader scope, revealing rainfall variability and making it particularly useful for understanding how specific years or events deviate within the complete record. The MRAI can highlight relative shifts across an entire timeline, offering insight into years with exceptionally high or low rainfall in a broader historical context. The MRAI is presented in Equation 2.

$$MRAI = \begin{cases} 3\left(\frac{P_n - \overline{P}}{P_{max} - \overline{P}}\right) & \text{if } P > \overline{P}, \\ -3\left(\frac{P_n - \overline{P}}{P_{min} - \overline{P}}\right) & \text{if } P < \overline{P} \end{cases} \quad (2)$$

Where P_{max} is the maximum precipitation value in the *n* series, and P_{min} is the minimum precipitation. Equation 2 ensures a comprehensive account of the anomalies from the actual rainfall extremes by considering both ends of the value spectrum.

3.4 *Calculating Standardized Rainfall Anomaly Index (SRAI)*

The National Weather Service (NWS) has recommended that an ideal RAI should incorporate standard deviation to capture deviations around the mean of the AMS (NOAA, 2017; NWS, 2020). However, a RAI model that includes standard deviation has yet to be implemented. This study introduces the concept of standard deviation to compute a Standardized Rainfall Anomaly Index (SRAI). The SRAI focuses on variability specifically around the standard deviation, which is particularly sensitive to extreme rainfall events. This makes the SRAI effective in detecting and quantifying the intensity and frequency of anomalous events relative to average conditions, with a particular emphasis on extremes. The SRAI index will be useful for identifying trends in the intensity of extremes, aiding in the assessment of shifts in the distribution of high-magnitude events that may indicate changing climatic patterns. The SRAI is presented in Equation 3.

$$SRAI = \begin{cases} 3\left(\left(\frac{P_n - \sigma}{P_{max} - \sigma}\right)\right) & \text{if } P > \overline{P}, \\ -3\left(\left(\frac{P_n - \sigma}{P_{min} - \sigma}\right)\right) & \text{if } P < \overline{P} \end{cases} \quad (3)$$

Where σ is the standard deviation from the *n* series of precipitation values.

3.5 *Fitting to Probability Distribution Function (PDF) and Kurtosis of indices*

The three anomaly indices (RAI, MRAI, and SRAI) were subjected to a probability density function (PDF) based on the Gumbel distribution to evaluate their effectiveness in estimating extreme rainfall anomaly scenarios. The Gumbel PDF was selected to fit the distributions of the indices following its suitability for extreme value representation and asymptotic distribution (Fadhel et al., 2017). Kurtosis was computed for all three anomaly indices and compared against normal distribution. The Gumbel PDF equation $F_1(x)$ is provided in Equation 4 below.

$$F_1(x) = \frac{1}{\sigma\sqrt{2\pi}}\exp\left(-\frac{1}{2}\left(\frac{x-\mu}{\sigma}\right)^2\right) \quad (4)$$

Where $F_1(x)$ represents the exceedance probability function of the Gumbel PDF, x denotes the AMS. The parameters μ_i and σ_i correspond to the parameters – mean and standard deviation of the theoretical distribution functions of the Gumbel PDF.

A reference normal distribution was derived based on the normal distribution from Equation 5 below. The normal distribution serves as a benchmark to assess the characteristics of the indices.

$$F_2(x) = \exp\left[-\exp\left(-\frac{x-\xi_1}{\alpha_1}\right)\right] \quad (5)$$

Where $F_2(x)$ represents the exceedance probability function of the Normal distribution, x denotes the AMS. The parameters ξ_i and α_i correspond to the parameters (mean and standard deviation) of the theoretical distribution functions of the Normal distribution. Kurtosis for all three anomaly indices was computed based on the general kurtosis equation presented in Equation 6. The kurtosis values generally ranged from -1 to +1. Kurtosis values around 0 indicate a normal

distribution, as expected. Values greater than 0 suggest positive kurtosis, indicating a more peaked distribution with a higher likelihood of estimating extreme rainfall events. Conversely, values less than 0 depict negative kurtosis, implying a flatter distribution with a reduced tendency to capture extreme events (Bono et al., 2020; Klima, 2021).

$$k = \mathrm{E}\left[\left(\frac{x-\mu}{\sigma}\right)^4\right] = \frac{\mathrm{E}[(x-\mu)^4]}{(\mathrm{E}[(x-\mu)^2])^2} \quad (6)$$

Where k represents the kurtosis estimate, x denotes the AMS. The parameters μ_i and σ_i are the mean and standard deviation. Figure 2 shows the comparison of Normal, positive, and negative kurtosis. A negative kurtosis (blue) produces a flatter curve and lies below the normal kurtosis (green), and when anomaly index type portrays such characteristics, it may not properly reflect extreme events. On the other hand, a positive kurtosis (red) peaks above the normal curve and suitably captures extreme anomaly events (Bono et al., 2020; Raziei, 2021). The summary workflow illustrates the IMERG AMS extraction, anomalies derivation, fitting to PDF, and evaluation of indices are presented in Figure 3.

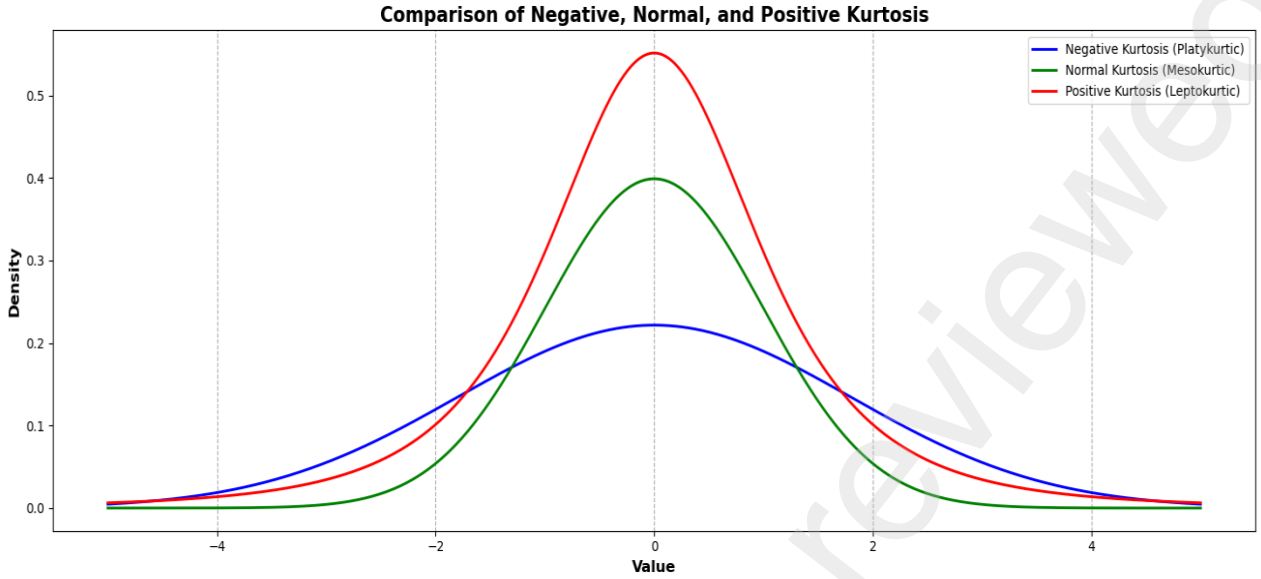

315

316 **Figure 2**. Ideal distributions for varying ranges of kurtosis. The positive distribution (red) above the
317 normal curve (green) tends to capture extremely wet conditions, while the negative, flatter distribution
318 (blue) below the normal curve captures extremely dry conditions.

319

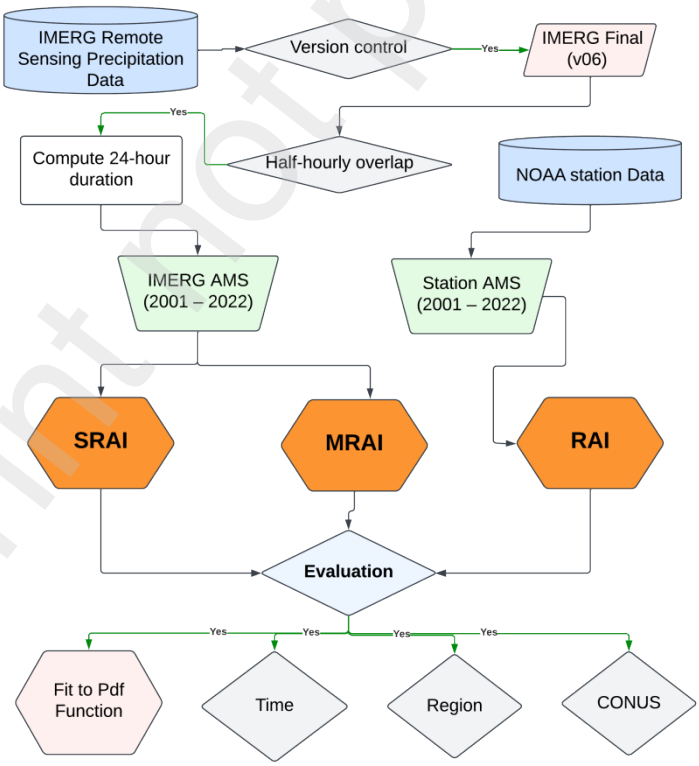

320

Figure 3. Summary workflow for modeling the proposed indices (MRAI and SRAI).

3.6 *Evaluation Statistics*

The proposed rainfall anomaly indices (MRAI and SRAI), modeled from IMERG data, are evaluated against the RAI index derived from NOAA station data. To assess performance, six statistical metrics were used: Pearson correlation coefficient (CC), percentage relative bias (PRB), root mean squared error (RMSE), Mean Bias Ratio (MBR), Nash-Sutcliffe Efficiency (NSE), and Kling-Gupta Efficiency (KGE) (Table 3). The mathematical formulations, value ranges, optimal value thresholds, and units for each evaluation metric are detailed in Table 3, where O represents the reference RAI index values across the years (2001–2022) and P represents the proposed indices (MRAI and SRAI).

Table 3. Statistical metrics for evaluating the indices (MRAI and SRAI). ***O*** is the reference RAI index, ***P*** are the proposed indices (MRAI and SRAI), N is a set 2360 stations, $\boldsymbol{\mu}$ is the mean, ***S*** standard deviation.

Statistics	Formula	Range	Optimal Value	Unit
Correlation Coefficient (CC)	$CC = \frac{\sum_{n\in\mathbf{N}}(P_n-\overline{P})(O_n-\overline{O})}{\sqrt{\sum_{n\in\mathbf{N}}(P_n-\overline{P})^2}\sqrt{\sum_{n\in\mathbf{N}}(O_n-\overline{O})^2}}$	-1 to 1	1	Unitless
Percentage Relative Bias (PRB)	$PRB = 100\times\frac{\sum_{n\in\mathbf{N}}(P_n-O_n)}{\sum_{n\in\mathbf{N}}O_n}$	-∞ to +∞	0	%
Root Mean Square Error (RMSE)	$RMSE = \sqrt{\frac{\sum_{n\in\mathbf{N}}(P_n-O_n)^2}{\lvert\mathrm{N}\rvert}}$	0 to +∞	0	Unitless
Mean Bias Ratio (MBR)	$MBR = \frac{\mu_P}{\mu_O}$	0 to 1	1	Unitless
Nash-Sutcliffe Efficiency (NSE)	$NSE = 1-\frac{\frac{1}{n}\sum_{i=1}^{n}(P_n-O_n)^2}{\frac{1}{n-1}\sum_{i=1}^{n}(O_n-\mu_O)^2}$	0 to 1	1	Unitless
Kling-Gupta Efficiency (KGE)	$KGE = 1-\sqrt{\left(1-\frac{S_P}{S_O}\right)^2+\left(1-\frac{\mu_P}{\mu_O}\right)^2+(1-\rho)^2}$	-∞ to 1	1	Unitless

4 **Results and Discussions**

4.1 *Comparing PDFs from anomaly indices*

Figure 4 depicts the PDFs of the RAI (in red), MRAI (in blue), and SRAI (in green), compared against the Normal PDF (dark broken line) from 2,360 stations across multiple years (2001–2022). As observed, over the years, the MRAI index recorded a more peaked distribution compared to the RAI and SRAI. When comparing the indices with the normal distribution, we find that all three indices (RAI, MRAI, and SRAI) exhibit elevated peaks, except for the years 2004 and 2022, where both RAI and SRAI fell below the normal distribution curve. The higher peaked curves above the normal suggest a tendency for these particular index models to capture extreme value rainfall statistics associated with positively skewed anomalies. To support these findings, kurtosis values were computed for all three indices and illustrated in Figure 5. Kurtosis values around 0 indicate a normal distribution, suggesting that the index may not properly capture both extreme (extremely dry and extremely wet) conditions. Values greater than 0 indicate a positive kurtosis, suggesting a more peaked distribution with a higher likelihood of estimating extreme rainfall events, thereby allowing the index to capture extremely wet anomalies. Conversely, values less than 0 indicate a negative kurtosis, implying a flatter distribution with less tendency to capture extreme events, thus enabling the index to capture extremely dry anomalies (Bono et al., 2020; Klima, 2021).

Figure 5 provides additional statistical insights into Figure 4, revealing that the MRAI has a higher propensity to capture extreme positive rainfall anomalies (i.e., extremely wet conditions) compared to the conventional RAI index, which exhibited a kurtosis value around 0. In contrast, the SRAI demonstrated a greater capacity to capture severely negative rainfall anomalies (i.e., extremely dry conditions) compared to the MRAI and RAI indices. Together,

Figures 4 and 5 illustrate the strengths of the proposed indices (MRAI and SRAI) in relation to the existing RAI index, providing users with ample opportunity to determine which set of indices best suits their specific needs. For research focused on capturing extreme wet conditions, the MRAI may be a superior choice compared to the existing RAI index due to its ability to capture extreme rainfall statistics in extremely wet areas, while the SRAI may be more appropriate when the goal is to analyze extreme rainfall statistics in an extremely dry area.

Raziei (2021), in an earlier attempt to simplify the RAI index using rainfall records from 45 stations in Iran, modeled the simplified standardized precipitation index (SSPI). Although the strength of the SSPI was primarily aimed at detecting extreme dry anomaly conditions in the Middle East, the study indicated that the existing RAI index, when fitted to a Gumbel PDF distribution, was close to the normal distribution PDF curve. This observation is consistent with the findings of this research. The RAI index in Figure 4 is normally distributed compared to the MRAI and SRAI indices, which aligns with Raziei (2021). The PDF distribution outcomes for both MRAI and SRAI indices were within expectations, demonstrating a tendency to capture extreme rainfall anomaly statistics that occur at both ends of the anomaly spectrum (extremely dry vs. extremely wet). The kurtosis of the MRAI index ranged from 0 to +0.9, while the SRAI exhibited kurtosis values between -0.9 and -0.1.

The kurtosis distribution and statistical insights for extreme rainfall anomalies provide practical implications for understanding and adapting to climate change, particularly regarding flood and drought risk management, agricultural practices, and community resilience. Higher kurtosis values for the MRAI index indicate an ability to capture extreme wet conditions, which is critical for forecasting and preparing for flood-related disasters. Conversely, the SRAI index, with negative kurtosis values, is better suited for identifying extreme dry conditions, informing

drought preparedness strategies. By understanding these extreme conditions more accurately, communities can be better prepared for the impacts of climate change on water availability, particularly in regions where rainfall patterns are increasingly unpredictable and extreme (Ahn et al., 2014; Pilgrim & Cordery, 1975; Viglione & Blöschl, 2009; Wasko et al., 2023). Emergency management agencies and policymakers could leverage these indices to create tailored responses for regions prone to floods or droughts, promoting resilience through improved infrastructure planning, resource allocation, and early warning systems.

In similar domains like agriculture, the ability to distinguish between extreme wet and dry anomalies is essential for crop planning and water resource management (Bedane et al., 2022; Zachariah et al., 2020; Zaveri et al., 2020). The MRAI's tendency to capture extreme wet events could aid in planning for crop selection and irrigation needs in flood-prone areas, potentially reducing crop losses during heavy rainfall seasons. Similarly, the SRAI's insights into extreme drought conditions can help farmers adopt drought-resistant crops or water-saving practices, promoting agricultural sustainability in dry regions. These indices allow agricultural stakeholders to make data-driven decisions, aligning their practices with climate variability and mitigating the economic impacts of climate extremes. By selecting indices tailored to specific rainfall anomalies, regions can better adapt their agricultural and community planning strategies, thereby enhancing food security and economic stability amidst the challenges posed by climate change.

The practical implications of using the MRAI and SRAI indices extend to broader climate change monitoring and adaptation strategies, as these indices help capture shifts in rainfall patterns, such as the increasing frequency of extreme wet and dry days, which are expected outcomes of climate change. By utilizing these indices, climate scientists and policymakers can

detect trends in anomalous rainfall days, which provides a clearer picture of changing precipitation patterns, especially under extreme conditions. The MRAI's capacity to identify more frequent extreme wet days aligns with the observed trend toward more intense rainfall events, which has been linked to global warming and atmospheric instability. By identifying and quantifying these trends, communities can bolster flood mitigation measures, such as constructing more efficient drainage systems, enhancing reservoir capacities, and planning urban spaces to reduce flood risks.

Similarly, the SRAI's strength in capturing extremely dry days provides essential insights for regions likely to experience extended droughts due to climate change. As climate models project an increased likelihood of prolonged dry spells in some regions, the SRAI index allows for proactive measures, such as optimizing water storage, implementing drought-resistant agricultural practices, and preparing for water scarcity by regulating consumption. These indices are valuable for early-warning systems, offering a predictive element that empowers communities to respond to both emerging and future climate risks. By continuously monitoring MRAI and SRAI trends, climate adaptation strategies can be refined and made more responsive, enabling the tracking of both immediate and long-term shifts in rainfall patterns due to climate change and facilitating resilient planning across vulnerable sectors, from agriculture to urban infrastructure.

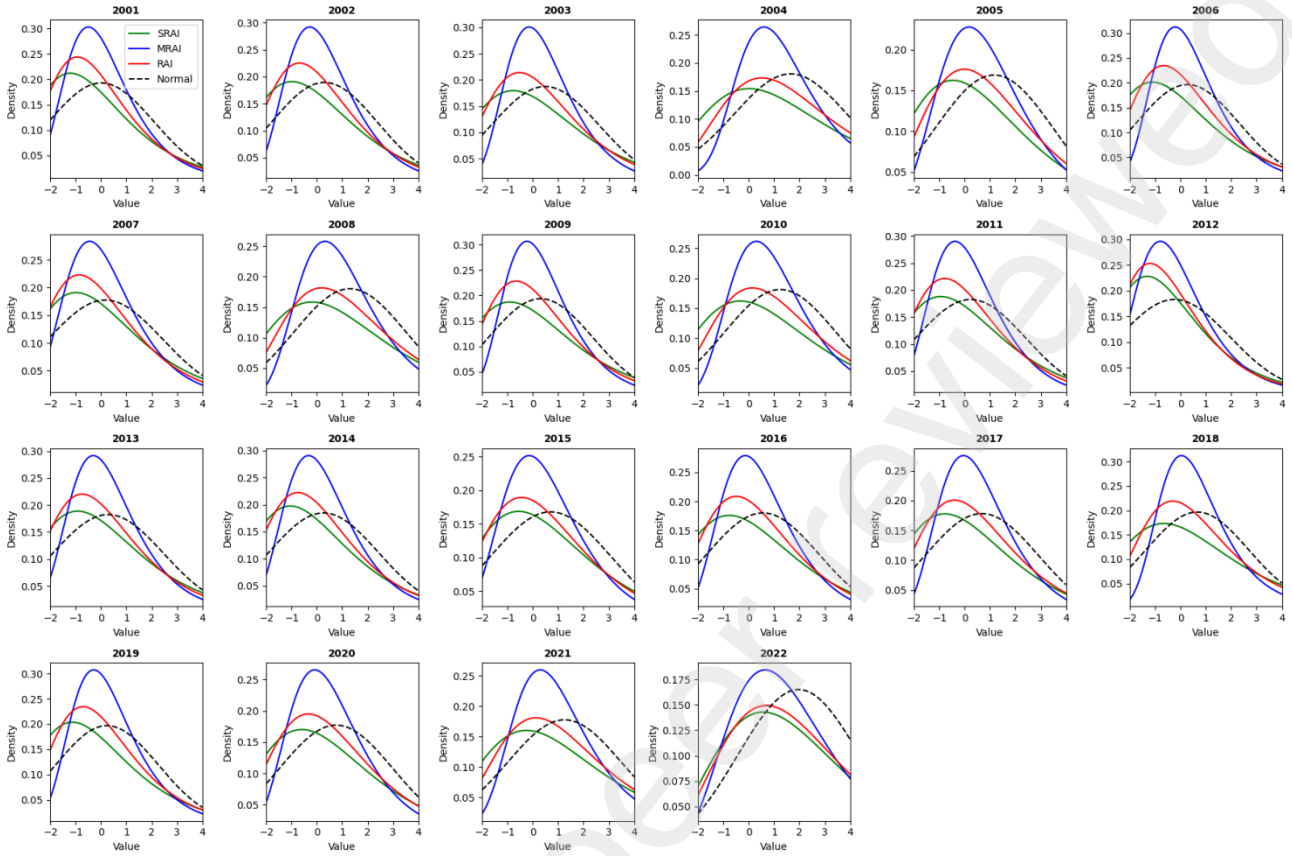

Figure 4. PDF distributions for the three anomaly indices: RAI (red), MRAI (blue), and SRAI (green), compared to the normal distribution (dark dashed line).

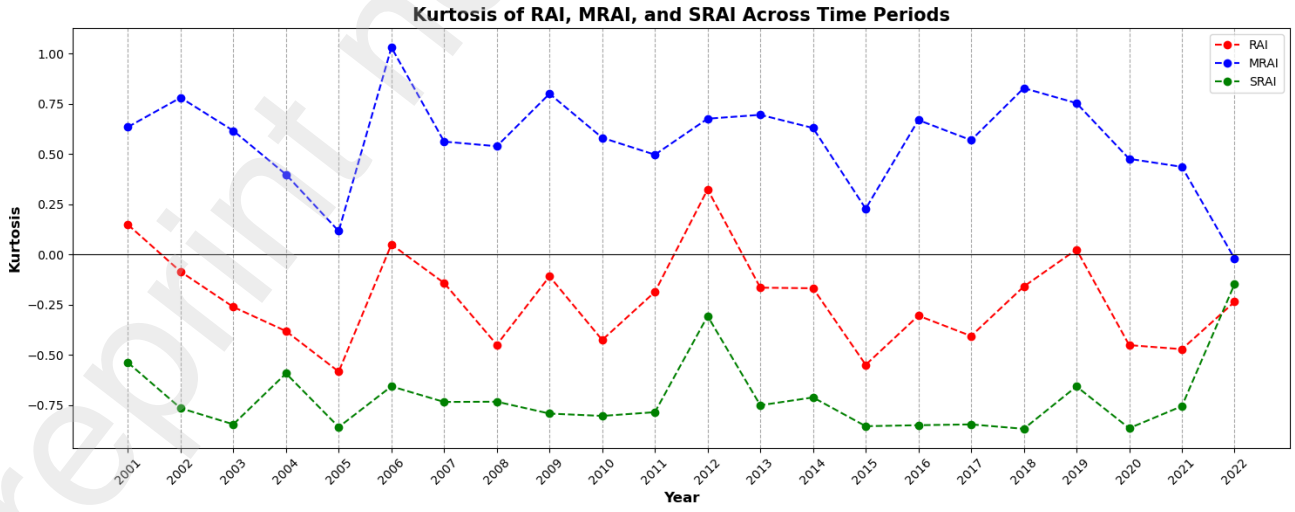

Figure 5. Kurtosis estimates for the three anomaly indices: RAI (red), MRAI (blue), and SRAI (green). These estimates were calculated using yearly anomaly index values from 2,360 stations.

4.2 *Comparing time variability of the indices*

The time variability of the median values is compared for the three indices. Figure 6 presents a box-plot comparison of the median anomaly index for all three indices by year. Across the years from 2001 to 2022, the median range of the SRAI index was between -2 and 0, the MRAI median index ranged from 0 to +2, while the median index value for the RAI was between -1 and +1. Figure 6 suggests that the MRAI tends to estimate extremely wet anomaly conditions, whereas the SRAI captures extremely dry conditions. Interestingly, all three indices exhibit a similar pattern, showing a rising and falling trend over the years, with a consistent increase from 2014 to 2022, indicating an increase in annual maximum rainfall depth in recent years. The observed increase in rainfall depth across CONUS, particularly in recent years, has been noted in earlier studies (Arias et al., 2012; Henny et al., 2023; Nasta et al., 2020).

Henny et al. (2023), in a recent study assessing the impacts of a warming global climate on seasonal large-scale extreme precipitation in CONUS, demonstrated that warming global temperatures between 2007 and 2019 are responsible for increasing rainfall intensity, frequency, and depth across the United States. Nasta et al. (2020), in a related study examining the impact of seasonal rainfall, found that changing climate conditions have led to increased rainfall frequency and intensity globally between 2010 and 2018. Several other studies have analyzed rainfall anomaly indices across various regions and found a subtle but increasing rainfall trend in recent years (Arias et al., 2012; Córdova et al., 2022; Huang et al., 2021; S. Wang et al., 2019).

Through this study, we not only observed the increasing trend in rainfall anomaly estimates in recent years but also demonstrated how various rainfall indices capture these anomalies, thereby revealing their strengths and weaknesses. The findings regarding the median observed rainfall indices are supported by earlier studies. For instance, Raziei (2021) found that the

median range of the RAI index was between -0.5 and +0.5, with a flexible range between -1 and +1. In this study, we observed a consistent range of -1 and +1 across the years 2001 to 2022. To support the observations in Figures 4 and 5, this study showed that the MRAI and RAI indices may be suitable for extremes that are not ideally computable using the RAI approach, with the MRAI tending toward extremely wet observations and the SRAI tending toward extremely dry observations. Combining the three indices provides an opportunity to conveniently monitor extreme rainfall anomalies worldwide, making this fusion vital for climate change studies concerning extreme drought and precipitation.

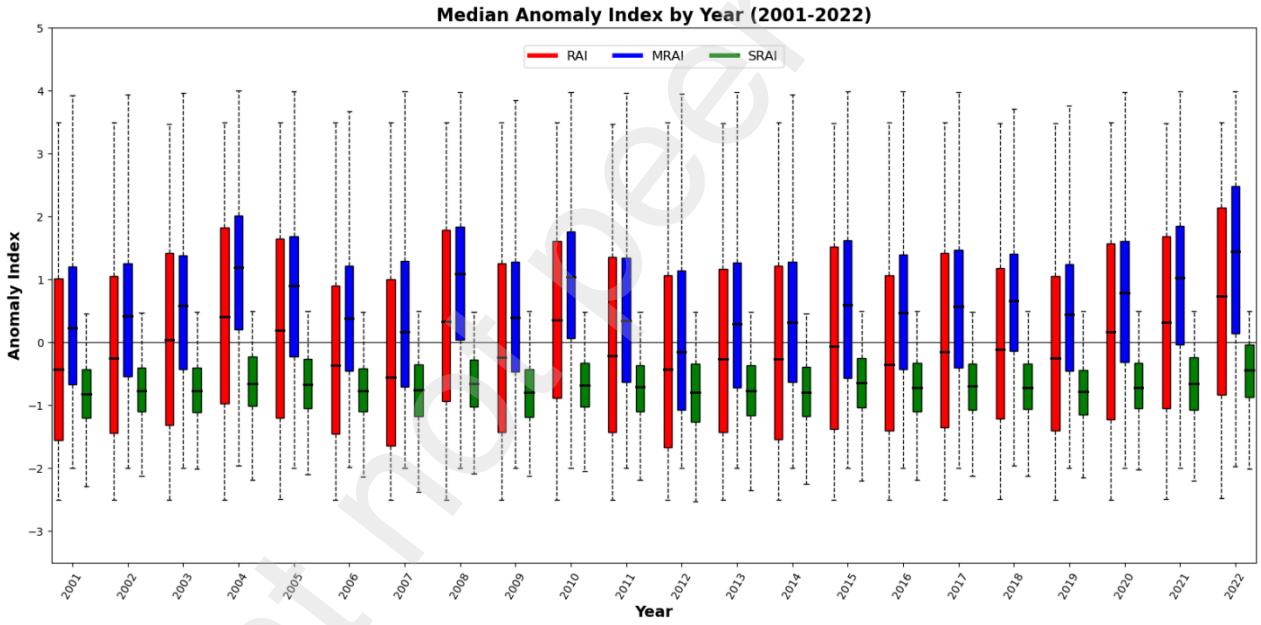

Figure 6. Assessment of the median distribution for the three anomaly indices: RAI (red), MRAI (blue), and SRAI (green). The median distributions are derived from yearly anomaly index values across 2,360 stations.

The revised indices (MRAI and SRAI) computed from IMERG data for the 2,360 stations were directly compared with the standard RAI index computed from NOAA gage data across multiple years from 2001 to 2022. Figure 7 presents the direct comparison between the MRAI (y-axis) and RAI (x-axis) indices for the years 2001 to 2022. The relationship exhibited a strong

positive correlation coefficient (CC) value ranging from 0.93 to 0.95 [2001 to 2022], with an average CC of 0.946. The SRAI index was also evaluated against the RAI across the same set of stations for the years 2001 to 2022 (Figure 8). The relationship between SRAI and RAI showed a CC ranging from 0.68 to 0.85, with an average CC of 0.71, indicating a stronger relationship between the MRAI and RAI indices than between the SRAI and RAI indices.

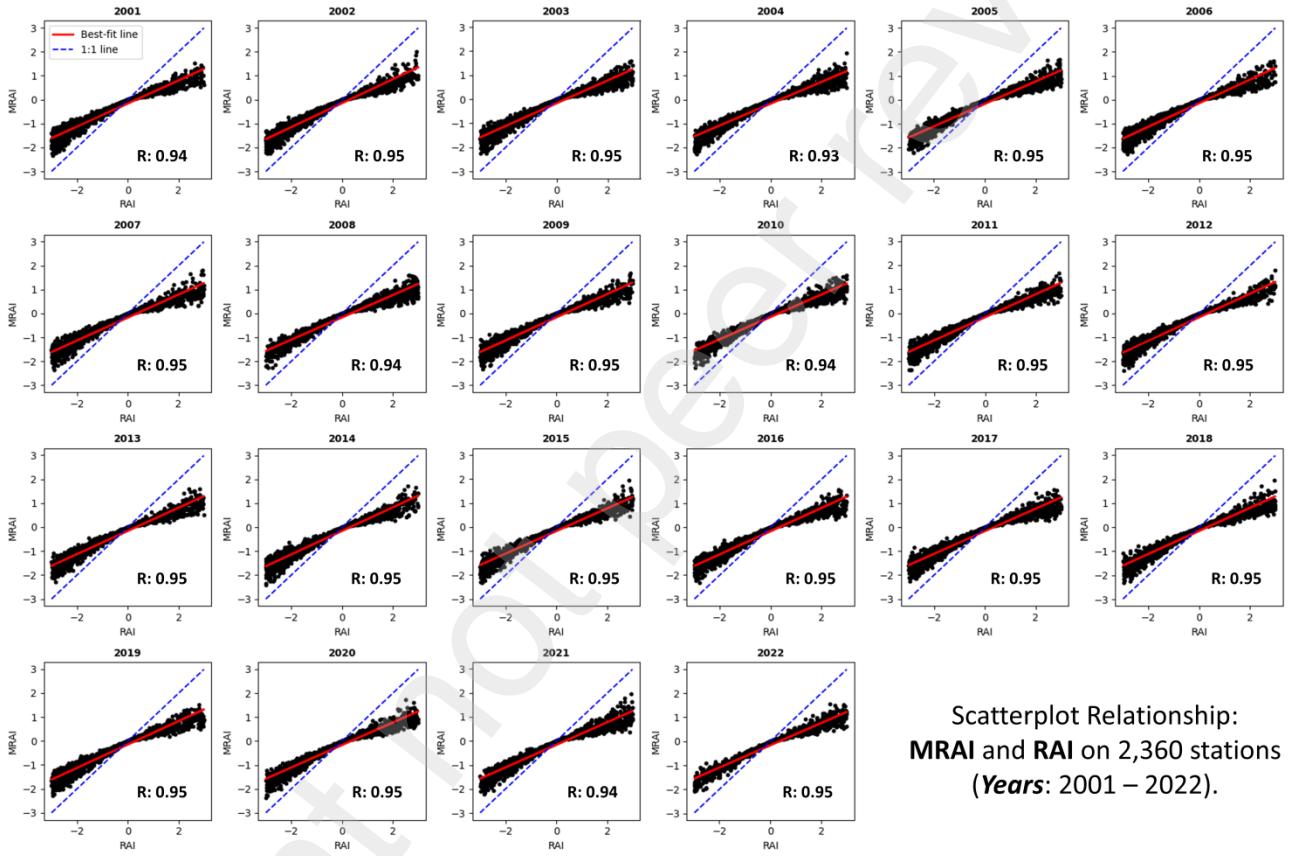

Figure 7. Relationship between the MRAI (y-axis) and RAI (x-axis) indices for the years 2001–2022. The computed anomalies are based on daily annual maximum rainfall estimates from 2,360 stations.

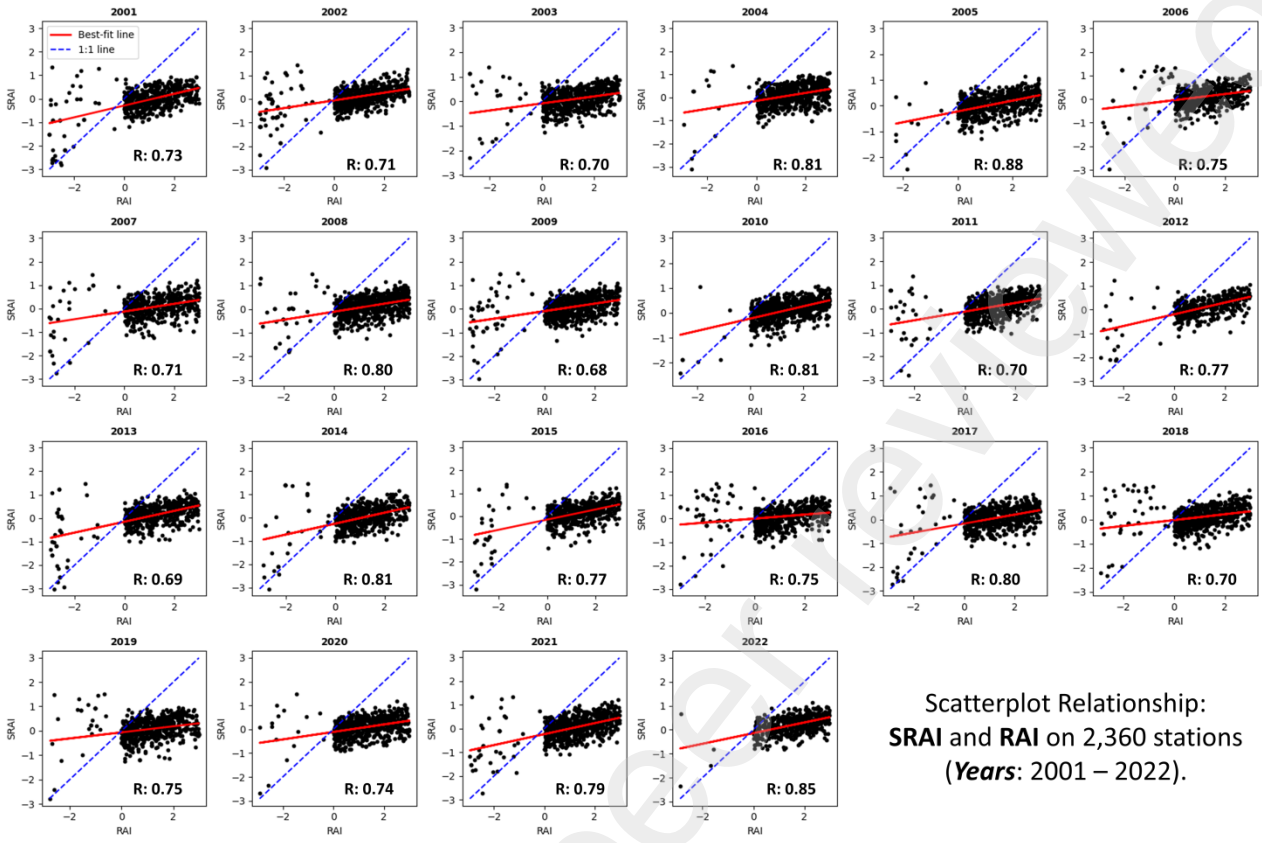

Figure 8. Relationship between the SRAI (y-axis) and RAI (x-axis) indices for the years 2001–2022. The computed anomalies are based on daily annual maximum rainfall estimates from 2,360 stations.

The full statistical evaluation over time is presented in Table 4. The relationship between MRAI and RAI showed an average statistic: CC estimate of 0.946, PRB estimate of -23.5, RMSE estimate of 0.93, MBR estimate of 0.74, NSE estimate of 0.82, and KGE estimate of 0.53. In contrast, the relationship between the SRAI and RAI indices was quite different, with average statistics showing: CC at 0.76, PRB at -14.5, RMSE at 1.7, MBR at 0.8, NSE at 0.41, and KGE at 0.46 across the years. These results clearly indicate a stronger agreement between the MRAI and RAI indices than between the SRAI and RAI indices when compared over the same time scale.

The observation that MRAI and RAI have a stronger agreement is not surprising, as earlier work by Raziei (2021) showed that RAI and SSPI—a similar approach to MRAI that uses

the 5th and 95th percentiles of the values rather than the minimum and maximum values from the full data range – reported a strong agreement (>0.85) across multiple durations of rainfall. The SRAI demonstrated a good agreement with RAI, with an average CC of 0.76, suggesting its usefulness alongside MRAI.

Table 4. Statistical results comparing MRAI and SRAI against RAI across the time intervals (2001–2022).

	MRAI						***SRAI***					
Year	**CC**	**PRB**	**RMSE**	**MBR**	**NSE**	**KGE**	**CC**	**PRB**	**RMSE**	**MBR**	**NSE**	**KGE**
2001	0.943	-16.289	0.898	0.837	0.812	0.632	0.728	9.319	1.709	1.000	0.319	0.658
2002	0.950	-16.048	0.872	0.840	0.828	0.642	0.712	11.030	1.799	1.000	0.270	0.634
2003	0.950	-4.297	0.957	0.957	0.798	0.621	0.701	7.200	1.840	1.000	0.253	0.639
2004	0.928	-48.600	1.051	0.514	0.774	0.408	0.812	-54.213	1.506	0.458	0.536	0.413
2005	0.946	-69.503	0.896	0.305	0.856	0.261	0.879	-200.031	1.291	0.000	0.701	-1.007
2006	0.949	-21.060	0.883	0.789	0.811	0.596	0.754	30.794	1.664	1.000	0.329	0.543
2007	0.946	-14.035	0.935	0.860	0.827	0.657	0.712	-5.907	1.834	0.941	0.334	0.680
2008	0.941	-79.424	0.981	0.206	0.804	0.141	0.800	-70.626	1.537	0.294	0.518	0.254
2009	0.948	-15.275	0.908	0.847	0.806	0.611	0.677	1.465	1.884	1.000	0.163	0.609
2010	0.943	-85.573	0.968	0.144	0.807	0.082	0.809	-123.965	1.525	0.000	0.521	-0.263
2011	0.949	-11.410	0.930	0.886	0.819	0.644	0.703	-4.557	1.847	0.954	0.286	0.660
2012	0.949	-15.012	0.846	0.850	0.849	0.694	0.772	-0.523	1.566	0.995	0.485	0.749
2013	0.951	-17.924	0.899	0.821	0.831	0.636	0.690	-0.163	1.880	0.998	0.262	0.654
2014	0.951	-15.358	0.899	0.846	0.827	0.641	0.806	19.284	1.488	1.000	0.526	0.688
2015	0.949	10.431	0.942	1.000	0.843	0.686	0.766	-3.803	1.705	0.962	0.485	0.748
2016	0.945	-7.096	0.930	0.929	0.823	0.669	0.749	14.970	1.739	1.000	0.383	0.662
2017	0.947	-4.601	0.932	0.954	0.827	0.675	0.796	62.908	1.579	1.000	0.503	0.323
2018	0.953	3.221	0.925	1.000	0.792	0.608	0.698	19.715	1.842	1.000	0.175	0.558
2019	0.946	-15.219	0.902	0.848	0.802	0.610	0.752	27.942	1.649	1.000	0.337	0.567
2020	0.946	40.859	0.962	1.000	0.817	0.472	0.745	38.077	1.743	1.000	0.400	0.522
2021	0.944	-83.789	0.980	0.162	0.810	0.099	0.789	-87.751	1.584	0.122	0.503	0.090
2022	0.948	-30.055	0.875	0.699	0.869	0.648	0.849	-8.412	1.348	0.916	0.690	0.826
min	**0.928**	**-85.573**	**0.846**	**0.144**	**0.774**	**0.082**	**0.677**	**-200.031**	**1.291**	**0.000**	**0.163**	**-1.007**
max	**0.953**	**40.859**	**1.051**	**1.000**	**0.869**	**0.694**	**0.879**	**62.908**	**1.884**	**1.000**	**0.701**	**0.826**
average	**0.946**	**-23.457**	**0.926**	**0.741**	**0.820**	**0.533**	**0.759**	**-14.420**	**1.662**	**0.802**	**0.408**	**0.464**

4.3 *Comparing variability of the indices with precipitation depth across time*

Comparing the rainfall anomaly indices with precipitation depth provides insights into how changes in precipitation might be captured by the indices. Figure 8 illustrates the relationship between the MRAI and RAI indices against the daily annual maximum rainfall depth from 2,360 stations across the years 2001 to 2022. Both MRAI and RAI exhibited consistent agreement with precipitation depth, with correlation coefficients (CC) ranging from 0.37/0.38 to 0.51/0.52 for the RAI and MRAI, respectively. With 2,360 stations covering 3,119,885 square miles of CONUS, the relationship between the indices and precipitation depth is considered high, with CC values greater than 0.4, particularly when accounting for uncertainties from the stations.

Similarly, the relationship between SRAI and precipitation (Figure 9) yielded CC values ranging from 0.23 to 0.55, with an average CC of 0.4 across the years 2001 to 2022. Although Raziei (2021) reported a higher CC range between RAI and precipitation depth (ranging from 0.97 to 1) across 45 stations, those results included several unresolved uncertainties due to the limited number of stations used. Consequently, the high CC values reported by Raziei (2021) are somewhat subjective. In contrast, this study utilized 2,360 stations, which increases the robustness of the analyses and reduces uncertainties arising from climate variability.

Figures 8 and 9 also demonstrate a strong correlation between the anomaly indices modeled from IMERG data (MRAI and SRAI) and those derived from NOAA station rainfall data (RAI) over the years. Notably, the CC relationship between MRAI modeled from IMERG data shows nearly a one-to-one correspondence with RAI modeled from NOAA station data (Figure 8), with a CC ratio of approximately 1. Meanwhile, SRAI from IMERG data exhibited a lower CC relationship with RAI from NOAA station data (Figure 9), with an average CC ratio of about 0.7.

518 The relationship between rainfall anomaly indices is crucial for end-users who rely on these
519 indices to plan and prepare for the impact of a changing climate. This study supports earlier
520 claims that remote sensing precipitation products like IMERG can aid locations lacking adequate
521 gaging networks in assessing rainfall anomalies. One significant application of the relationship
522 between anomaly indices and changes in depth in precipitation is in agriculture. Previous studies
523 have shown that farmers utilize these rainfall anomaly indices to predict crop yield performance
524 amid fluctuating rainfall intensities and frequencies (Gornall et al., 2010; Mohammadi et al.,
525 2023; Wilson et al., 2022). However, the focus has primarily been on rainfall deficits (droughts)
526 with less attention on rainfall surpluses (H. Chen et al., 2023; K. O. Ekpetere et al., 2024;
527 Seleiman et al., 2021; Weng et al., 2023; Zachariah et al., 2020).

528 Recently, studies have begun to explore how surplus rainfall can impact crop productivity
529 (Bedane et al., 2022; Iizumi et al., 2024; Y.-U. Kim et al., 2024; Li et al., 2019). The revised
530 rainfall anomaly indices developed in this study will benefit both farmers and scientists
531 interested in assessing changes in rainfall deficits and surpluses, including hydrologists engaged
532 in flood forecasting (K. Ekpetere, 2024; LaRocque, 2013; VDCR, 2015; Zischg et al., 2018).
533 City planners can also enhance their community planning efforts by recognizing the full
534 spectrum of rainfall variations (Ahn et al., 2014; Boota et al., 2015; Fashae et al., 2017; Trinh et
535 al., 2022).

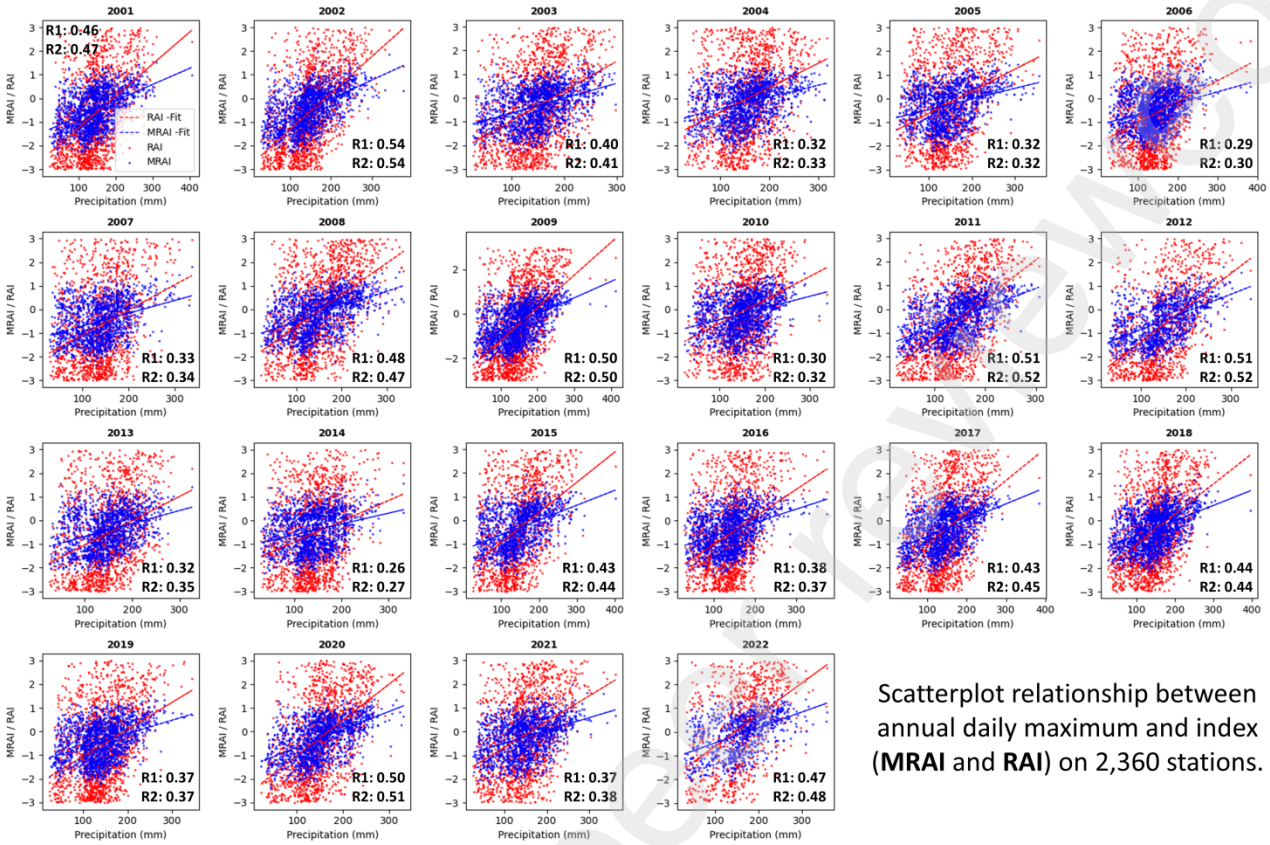

Scatterplot relationship between annual daily maximum and index (**MRAI** and **RAI**) on 2,360 stations.

536

537 **Figure 8**. Relationship between annual maximum rainfall depth (from 2,360 stations) and anomaly indices

538 (MRAI and RAI) across the years 2001–2022.

539

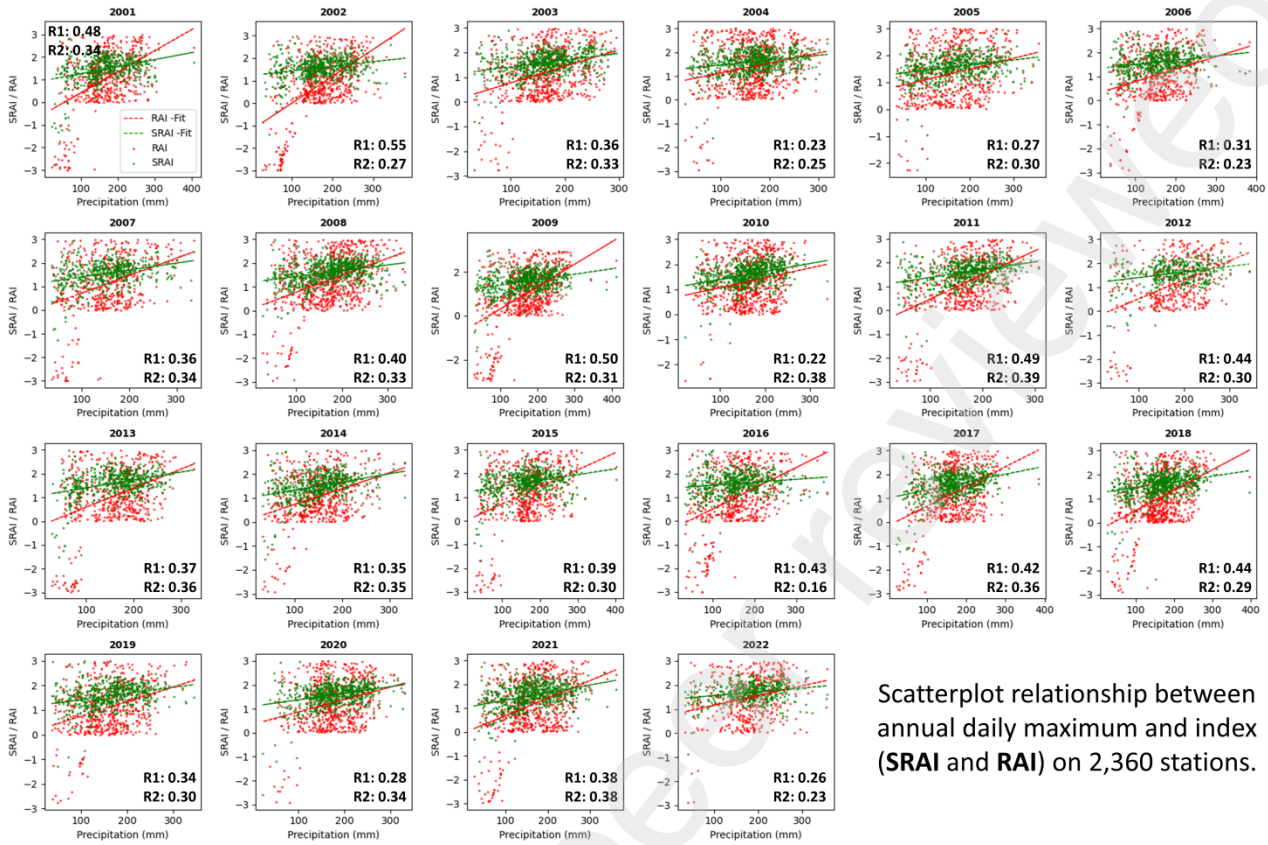

Scatterplot relationship between annual daily maximum and index (**SRAI** and **RAI**) on 2,360 stations.

Figure 9. Relationship between annual maximum rainfall depth (from 2,360 stations) and anomaly indices (SRAI and RAI) across the years 2001–2022.

4.4 *Performance of indices in extreme rainfall locations in CONUS*

The modeled indices (MRAI and SRAI) were evaluated in extreme climate regions within the CONUS to assess their performance in both extremely wet and extremely dry climates. Twenty stations were randomly selected from Louisiana and Nevada based on earlier extreme rainfall anomaly studies in CONUS. Armal & Khanbilvardi (2019) and Singh et al. (2020) identified Louisiana as having the highest annual rainfall depth and Nevada as having the lowest in recent years. The presence of the Mississippi River, susceptibility to tropical cyclones (Tibbetts, 2006), and dual rainy seasons (in spring and fall), along with an average rainfall depth

552 of 57.05 inches (Brown et al., 2020; Faiers et al., 1994), characterize Louisiana as a wet state. In
553 contrast, Nevada has recorded the lowest amounts of rainfall depth, intensity, and frequency over
554 the past decade (Pan et al., 2011; Z. Yu et al., 2015).

555 The MRAI and SRAI indices demonstrated a strong relationship with the RAI base index
556 in extremely wet locations (Figure 10). Across the 20 selected stations in Louisiana, the anomaly
557 trends between the indices followed similar patterns and were highly consistent. The statistics
558 presented in Table 5 show strong agreement between MRAI and RAI, with average statistics of
559 CC: 0.943, PRB: 0.075, RMSE: 0.923, MBR: 0.727, NSE: 0.815, and KGE: 0.036. Similarly,
560 the statistics for SRAI and RAI yielded average values of CC: 0.908, PRB: 1.38, RMSE: 1.21,
561 MBR: 0.865, NSE: 0.678, and KGE: -1.330. These results indicate a stronger relationship
562 between MRAI and RAI in extremely wet stations of Louisiana compared to the SRAI and RAI
563 comparison.

564 In the dry station locations of Nevada, MRAI showed close agreement with RAI, whereas
565 SRAI did not exhibit a consistent pattern with RAI (Figure 11). At many stations in Nevada,
566 SRAI peaked above the other indices, indicating a tendency to detect extreme fluctuations in low
567 rainfall trends. One important characteristic of the SRA index is its ability to capture extreme
568 rainfall anomalies in extremely dry locations, as demonstrated in Figure 11. The statistical
569 comparison between the advanced indices and RAI is presented in Table 6. For MRAI and RAI,
570 the average statistics were CC: 0.957, PRB: 0.133, RMSE: 0.887, MBR: 0.819, NSE: 0.841, and
571 KGE: 0.351. In contrast, for SRAI and RAI, the average statistics were CC: 0.582, PRB: -2.126,
572 RMSE: 2.074, MBR: 0.557, NSE: -0.119, and KGE: -3.841. These findings align with earlier
573 studies demonstrating the potential of satellite precipitation products to model rainfall anomalies
574 in extreme wet and dry conditions, such as those observed in California, Nevada, and Arizona

(Byrne et al., 2023; Faiers et al., 1994; L. Gu et al., 2023; Hoell et al., 2022; Hu et al., 2021; Z. Yu et al., 2015).

This work demonstrates that the use of IMERG data to model both MRAI and SRAI indices holds promise for wider evaluation in regions beyond CONUS. With nearly global coverage, IMERG will assist researchers and policymakers in effectively monitoring extreme events (Gavahi et al., 2022; Vicente-Serrano et al., 2010; Weng et al., 2023; G. Zhang et al., 2021; Y. Zhang et al., 2023). Furthermore, IMERG can be utilized to monitor anomalies arising from changes in the global climate (K. Ekpetere et al., 2022, 2023; Felder et al., 2019; Weng et al., 2023; Yuan et al., 2019).

The results of the MRAI and SRAI indices across regions with varied rainfall patterns highlight significant practical applications in fields like agriculture, urban planning, water resource management, and climate resilience. In areas with high rainfall, such as Louisiana, the MRAI's alignment with the RAI indicates its utility for identifying and preparing for extreme wet conditions. This capability is particularly beneficial in agriculture, where understanding periods of excessive rainfall can help farmers plan crop cycles, select flood-resistant crop varieties, and manage soil health to prevent waterlogging. Additionally, urban planners can utilize the MRAI to design more flood-resilient infrastructure by identifying trends in extreme rainfall events. This knowledge informs the construction of stormwater systems, drainage networks, and flood defenses, ultimately improving city resilience to high-intensity storms and minimizing property damage. Emergency management teams can also leverage the MRAI's insights for early warning systems, enabling timely evacuations and resource allocation during extreme weather events.

In arid regions, such as Nevada, the SRAI's capacity to capture extreme dry anomalies proves invaluable for water resource managers, who can use it to monitor drought onset and severity. This information enables better planning for water allocation, storage, and distribution, crucial for sustaining both municipal and agricultural water needs in drought-prone areas. The SRAI can also guide agricultural decisions in dry regions by helping farmers optimize water use and invest in drought-resistant crops, irrigation technologies, and soil conservation techniques, thus enhancing crop yields and financial stability under adverse conditions. Furthermore, the ability of MRAI and SRAI indices to detect rainfall extremes beyond CONUS regions, through globally applicable IMERG data, supports climate adaptation strategies in countries facing varying and intensifying rainfall patterns. Researchers and policymakers can use these indices to track climate change impacts on rainfall at a global scale, developing tailored climate-resilient policies for regions prone to either floods or droughts. This localized approach based on regional rainfall patterns allows for more effective allocation of resources, efficient disaster response planning, and a proactive stance in adapting to evolving climate realities.

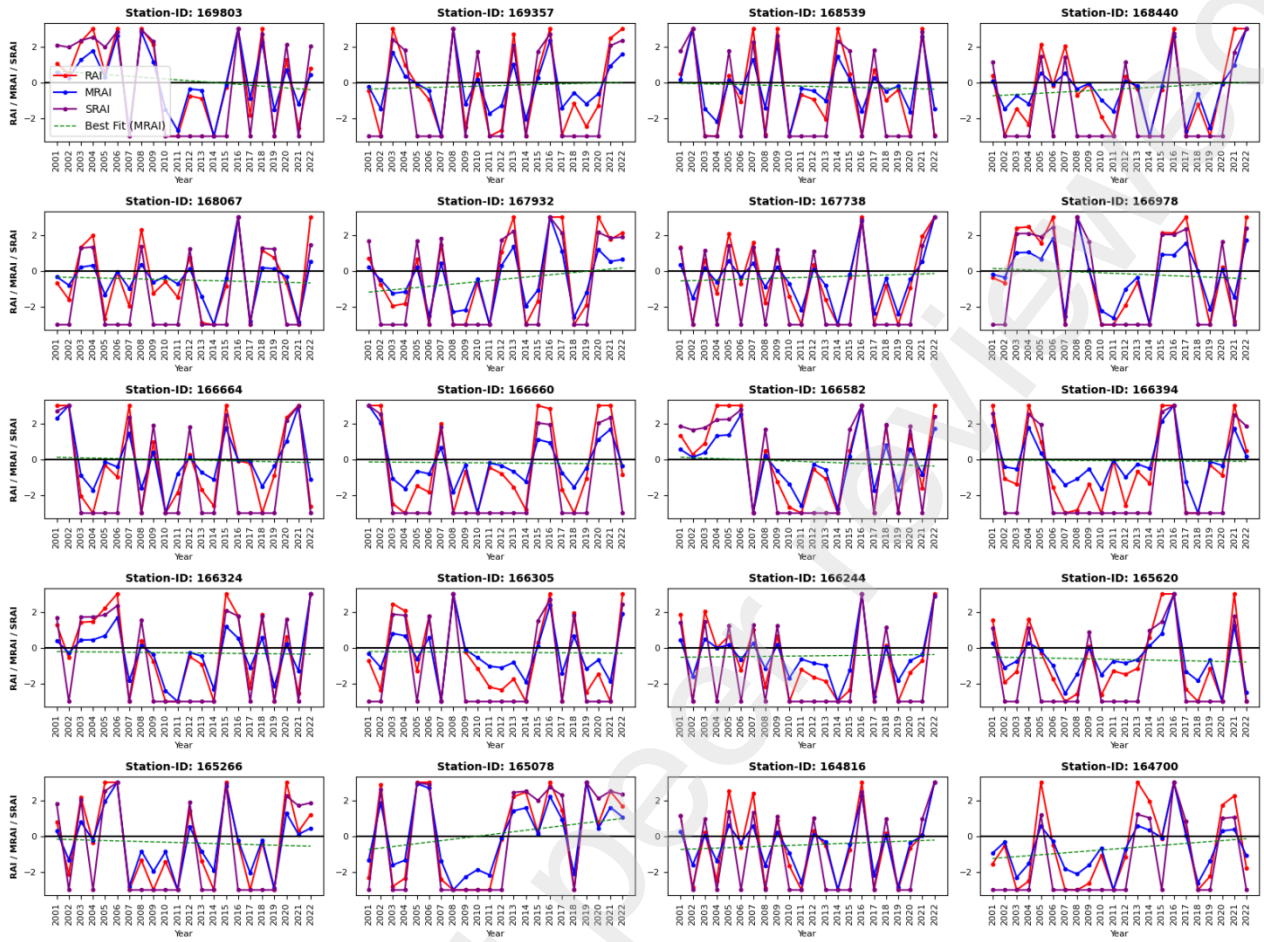

Figure 10. Variability assessment of the anomaly indices (MRAI, SRAI, and RAI) in the humid climate of Louisiana, based on selected stations.

Table 5. Statistical results comparing MRAI and SRAI against RAI across 20 selected stations in Louisiana.

Station-ID	*MRAI*						*SRAI*					
	CC	PRB	RMSE	MBR	NSE	KGE	CC	PRB	RMSE	MBR	NSE	KGE
169803	0.965	0.217	0.758	1.000	0.890	0.675	0.919	-1.532	1.097	0.000	0.769	-0.546
169357	0.950	-0.461	1.029	0.539	0.800	0.411	0.914	1.635	1.179	1.000	0.738	-0.641
168539	0.956	-0.536	0.949	0.464	0.822	0.371	0.898	0.914	1.214	1.000	0.709	0.068
168440	0.927	-0.186	0.878	0.814	0.811	0.648	0.849	2.291	1.580	1.000	0.388	-1.300
168067	0.880	0.175	1.013	1.000	0.724	0.599	0.883	2.155	1.389	1.000	0.481	-1.163
167932	0.958	0.581	0.952	1.000	0.825	0.329	0.937	1.251	0.967	1.000	0.820	-0.257
167738	0.938	-0.157	0.791	0.843	0.836	0.684	0.906	1.614	1.205	1.000	0.620	-0.628
166978	0.965	-3.145	0.890	0.000	0.851	-2.160	0.898	-7.231	1.241	0.000	0.710	-6.233
166664	0.951	-0.896	0.971	0.104	0.814	0.046	0.901	2.329	1.352	1.000	0.639	-1.336

166660	0.934	-0.435	1.152	0.565	0.753	0.402	0.940	2.723	1.284	1.000	0.693	-1.724
166582	0.955	4.796	0.876	1.000	0.848	-3.805	0.923	8.989	1.009	1.000	0.799	-7.991
166394	0.953	-0.820	1.009	0.180	0.783	0.104	0.898	1.890	1.396	1.000	0.584	-0.900
166324	0.947	1.516	0.951	1.000	0.807	-0.555	0.914	3.754	1.094	1.000	0.745	-2.758
166305	0.939	-0.456	1.023	0.544	0.783	0.416	0.935	1.395	1.110	1.000	0.744	-0.402
166244	0.934	-0.345	0.841	0.655	0.814	0.556	0.904	0.851	1.159	1.000	0.647	0.125
165620	0.926	-0.157	0.944	0.843	0.780	0.613	0.911	1.033	1.188	1.000	0.651	-0.038
165266	0.962	0.075	0.751	1.000	0.884	0.745	0.900	1.548	1.247	1.000	0.680	-0.560
165078	0.981	1.633	0.753	1.000	0.909	-0.652	0.954	-0.694	0.844	0.306	0.885	0.296
164816	0.939	-0.018	0.826	0.982	0.833	0.712	0.885	1.008	1.159	1.000	0.672	-0.021
164700	0.908	0.108	1.104	1.000	0.737	0.588	0.898	1.591	1.381	1.000	0.588	-0.595
min	**0.880**	**-3.145**	**0.751**	**0.000**	**0.724**	**-3.805**	**0.849**	**-7.231**	**0.844**	**0.000**	**0.388**	**-7.991**
max	**0.981**	**4.796**	**1.152**	**1.000**	**0.909**	**0.745**	**0.954**	**8.989**	**1.580**	**1.000**	**0.885**	**0.296**
average	**0.943**	**0.075**	**0.923**	**0.727**	**0.815**	**0.036**	**0.908**	**1.376**	**1.205**	**0.865**	**0.678**	**-1.330**

617

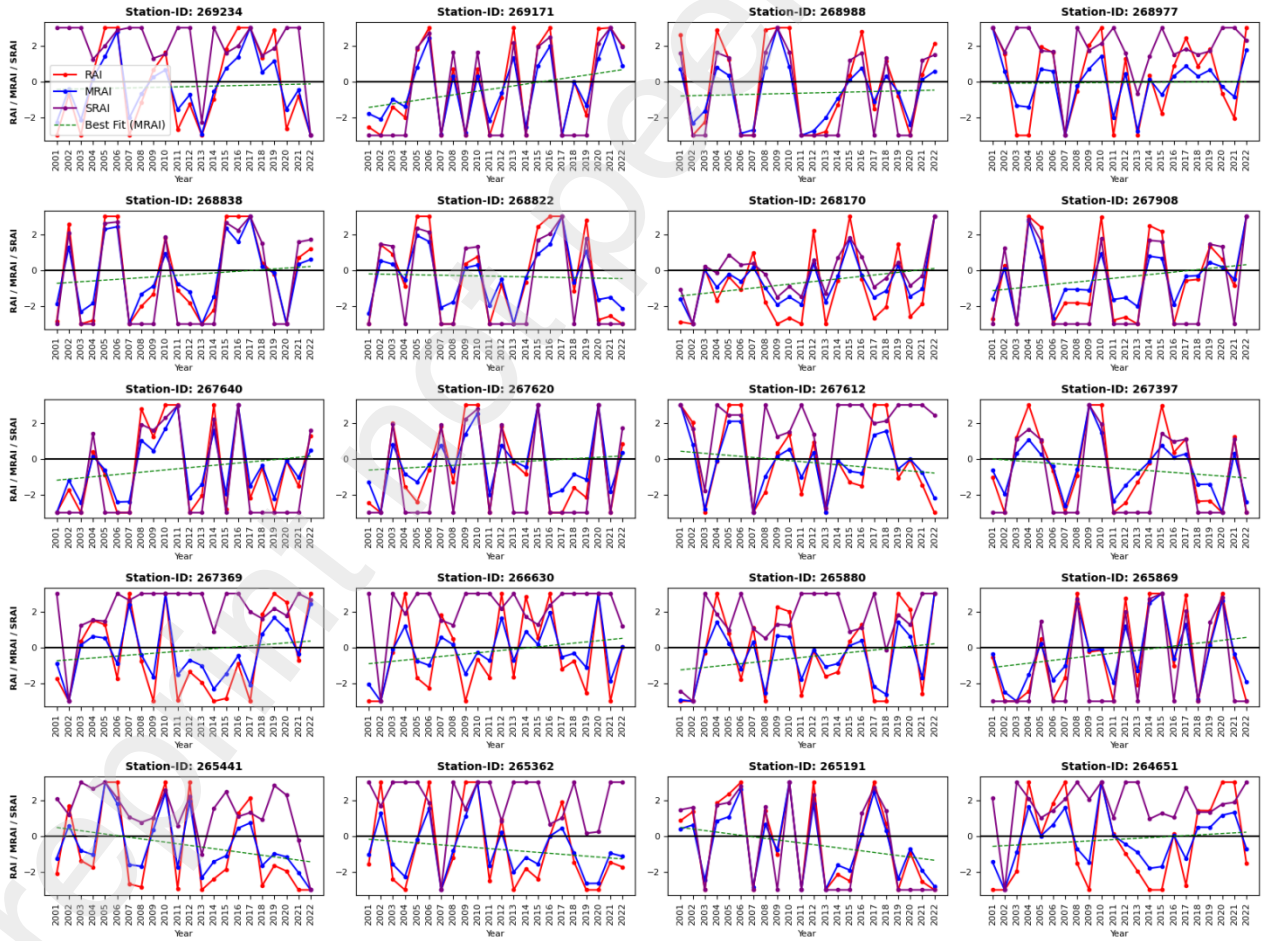

618

Figure 11. Variability assessment of the anomaly indices (MRAI, SRAI, and RAI) in the dry climate of Nevada, based on selected stations.

Table 6. Statistical results of MRAI and SRAI compared against RAI across 20 selected stations in Nevada.

Station-ID	*MRAI*						*SRAI*					
	CC	**PRB**	**RMSE**	**MBR**	**NSE**	**KGE**	**CC**	**PRB**	**RMSE**	**MBR**	**NSE**	**KGE**
269234	0.956	0.385	0.872	1.000	0.855	0.520	0.131	-10.612	3.414	0.000	-1.215	-9.652
269171	0.973	0.888	0.792	1.000	0.891	0.077	0.939	2.188	0.997	1.000	0.827	-1.190
268988	0.948	2.272	1.116	1.000	0.785	-1.297	0.943	2.597	0.949	1.000	0.844	-1.598
268977	0.933	-1.311	1.036	0.000	0.774	-0.361	0.138	10.020	2.948	1.000	-0.827	-9.064
268838	0.977	0.236	0.688	1.000	0.915	0.677	0.944	2.018	0.965	1.000	0.834	-1.021
268822	0.965	0.188	0.945	1.000	0.840	0.613	0.932	1.847	1.028	1.000	0.811	-0.848
268170	0.938	-0.333	0.943	0.667	0.769	0.514	0.870	-0.855	1.376	0.145	0.508	0.059
267908	0.938	-0.026	0.979	0.974	0.810	0.669	0.929	1.393	1.074	1.000	0.772	-0.396
267640	0.971	-0.056	0.759	0.944	0.892	0.740	0.923	1.050	1.119	1.000	0.766	-0.056
267620	0.957	-0.473	0.881	0.527	0.848	0.446	0.934	1.408	1.118	1.000	0.755	-0.417
267612	0.960	1.178	0.771	1.000	0.872	-0.206	0.382	-22.015	2.921	0.000	-0.833	-21.025
267397	0.945	0.231	0.936	1.000	0.813	0.591	0.911	1.680	1.183	1.000	0.701	-0.683
267369	0.960	-0.428	0.888	0.572	0.847	0.472	0.093	-7.397	3.563	0.000	-1.463	-6.464
266630	0.937	-0.369	1.025	0.631	0.777	0.470	-0.050	-8.050	3.652	0.000	-1.826	-7.127
265880	0.958	0.735	0.884	1.000	0.842	0.205	0.200	-6.005	3.088	0.000	-0.932	-5.063
265869	0.971	-0.256	0.730	0.744	0.900	0.654	0.900	1.870	1.318	1.000	0.674	-0.875
265441	0.967	-0.307	0.898	0.693	0.851	0.563	0.433	-2.993	2.969	0.000	-0.633	-2.072
265362	0.955	-0.058	0.880	0.942	0.837	0.674	0.001	-3.583	3.829	0.000	-2.080	-2.733
265191	0.984	0.461	0.595	1.000	0.936	0.503	0.959	0.721	0.752	1.000	0.897	0.274
264651	0.943	-0.307	1.111	0.693	0.767	0.488	0.121	-7.811	3.220	0.000	-0.956	-6.873
min	**0.933**	**-1.311**	**0.595**	**0.000**	**0.767**	**-1.297**	**-0.050**	**-22.015**	**0.752**	**0.000**	**-2.080**	**-21.025**
max	**0.984**	**2.272**	**1.116**	**1.000**	**0.936**	**0.740**	**0.959**	**10.020**	**3.829**	**1.000**	**0.897**	**0.274**
average	**0.957**	**0.133**	**0.887**	**0.819**	**0.841**	**0.351**	**0.582**	**-2.126**	**2.074**	**0.557**	**-0.119**	**-3.841**

4.5 *Spatial variability of the revised indices*

To assess the spatial variability of the three indices—MRAI, SRAI, and RAI—the average and median anomaly estimates were computed across the 2,360 stations from 2001 to 2022. Figure 12 illustrates the spatial distribution of the average anomalies from these indices mapped

for all 2,360 stations. A consistent pattern is observed between MRAI and RAI, in contrast to the mean anomalies from SRAI. Notably, SRAI exhibited elevated mean anomalies in regions with historically low precipitation, such as the arid western desert areas of Nevada and Arizona, alongside other locations with recorded fluctuations. This behavior aligns with earlier observations, where SRAI demonstrated a tendency to capture anomalies under extreme dry conditions.

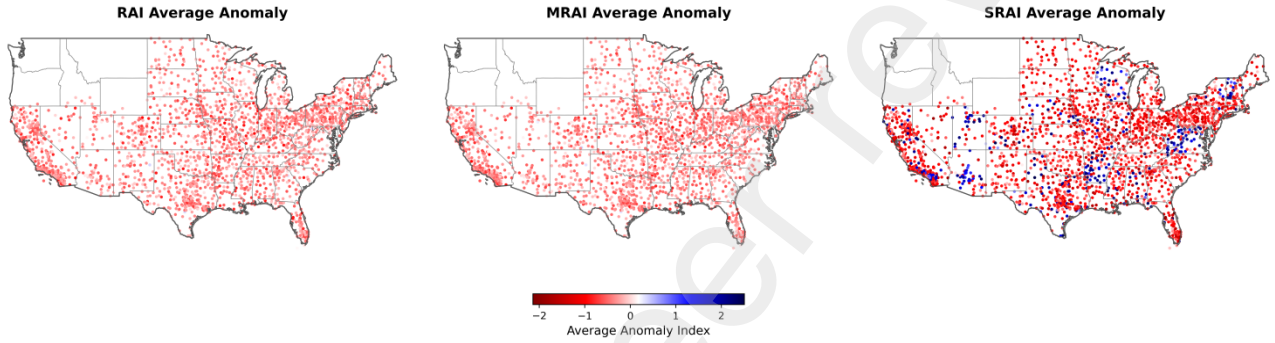

Figure 12. Spatial distribution of average anomaly indices (MRAI, SRAI, and RAI) across 2,360 stations in CONUS.

Similarly, the median values from the indices were compared spatially across the 2,360 stations in CONUS (Figure 13). The SRAI stands out due to its ability to detect extreme fluctuations in both directions of the anomaly spectrum (i.e., extremely dry and extremely wet conditions). The median anomaly estimates from the SRAI indicate that dry climate areas exhibited elevated positive anomalies, while known wet climate locations showed moderate to negative anomalies. This suggests that the SRAI tends to register higher anomalies in dry locations while capturing declines in rainfall that occur in wet climates. This observation aligns with earlier research, which demonstrated that anomaly indices can spike positively in dry regions following unexpectedly intense precipitation (Gershunov et al., 2019; McKitrick & Christy, 2019). Gershunov et al. (2019) utilized five rainfall projection models to demonstrate

that projected rainfall will increase across CONUS, with new indices capable of capturing slight fluctuations in dry regions extending beyond CONUS. While the MRAI and SRAI indices show promise for extreme rainfall studies, they will need to be tested across multiple stations outside CONUS to evaluate their applicability and limitations in different contexts.

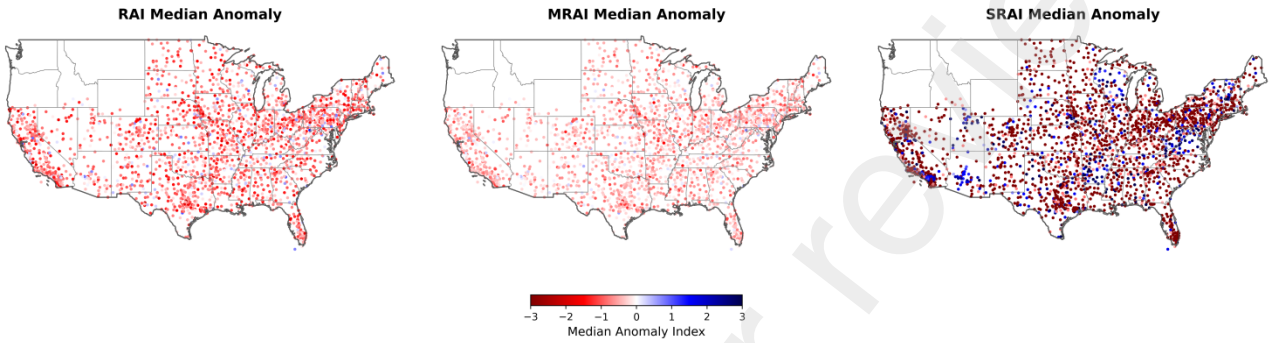

Figure 13. Spatial distribution of median anomaly indices (MRAI, SRAI, and RAI) across 2,360 stations in CONUS.

Figure 14 presents the statistics comparing MRAI and SRAI computed across the 2,360 stations to assess their spatial trends. CC ranges from ≥ 0.90, indicating a strong relationship between the two indices. The PRB is approximately 0, suggesting an unbiased estimate. The RMSE varies between 0.5 and 1.25, while the MBR falls between 0.5 and 1. The NSE ranges from 0.7 to 0.9, indicating a good predictive performance, although the KGE records values below 0. Overall, the analysis demonstrates a positive spatial agreement between MRAI and RAI, further suggesting that the MRAI index is likely to yield outcomes similar to those of the conventional RAI index.

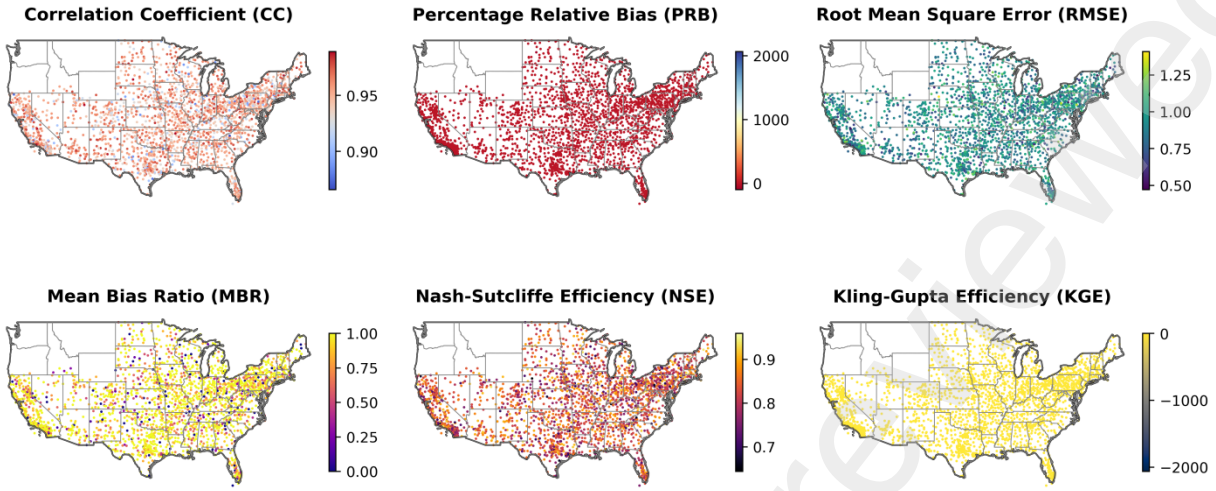

664

665 **Figure 14**. Spatial evaluation of the MRAI anomaly index across 2,360 stations in CONUS.

666

667 Similarly, Figure 15 presents the statistics comparing SRAI with RAI computed across
668 the 2,360 stations to assess the spatial trends between the indices. The CC ranges from 0.30 to
669 0.90, indicating variable agreement. The PRB is approximately 0, with a few exceptional outliers
670 falling below 0. The RMSE spans from 1 to 4, while the MBR ranges from 0 to 1. The NSE
671 averages around 0, with a few exceptions below 0, and the KGE is recorded as being below 0.
672 These statistics indicate a lower agreement between SRAI, and the RAI index compared to
673 MRAI; however, the overall trend suggests potential for the application of the SRAI index
674 model.

675 The integration of all three indices provides an opportunity to accurately model rainfall
676 anomalies by considering deviations from the mean and the standard deviation around the means.
677 Consequently, the combined indices will facilitate a proper representation of rainfall anomalies
678 in extreme environments experiencing severe droughts and prolonged intense rainfall events.
679 Both MRAI and SRAI demonstrate the capacity to model conditions effectively in extremely

wet and extremely dry environments, and when used in tandem, they complement each other. Temporally, across the years 2001 to 2022, and spatially across the 2,360 stations, the advanced indices (MRAI and SRAI) exhibit strong agreement and are capable of detecting extremes beyond the capabilities of the conventional RAI index.

The spatial variability observed in the MRAI, SRAI, and RAI indices across 2,360 stations in varying climate regions offers key insights for planning around extreme rainfall impacts. MRAI's consistency with RAI across the years indicates it effectively captures wet anomaly patterns in regions with high rainfall, which is crucial for flood-prone areas. MRAI's alignment with RAI in these wet regions means it can support flood risk assessment by predicting likely extreme rainfall events, enabling proactive measures such as urban drainage improvements, infrastructure reinforcement, and community readiness. The reliability of MRAI in capturing these wet anomalies allows urban planners and emergency management agencies to anticipate peak rainfall periods and develop pre-emptive responses, reducing flood impact and supporting resilience against intensifying climate variability.

On the other hand, SRAI's distinctive ability to capture anomalies in dry regions, especially in arid western areas like Nevada and Arizona, highlights its relevance in drought-prone areas. Elevated mean anomalies detected by SRAI in historically dry locations signal its usefulness for drought forecasting, supporting water resource management, and agricultural planning. The ability of SRAI to register both extreme wet and dry fluctuations means it can inform water conservation strategies and guide agricultural decisions in regions vulnerable to climate-induced dry spells. By detecting even slight precipitation spikes in typically dry regions, SRAI provides actionable insights for water managers and farmers to adapt to shifting rainfall patterns, making it a valuable tool in planning for both scarcity and surplus. The combined use

of MRAI and SRAI thus offers a comprehensive approach to managing extreme rainfall variability, providing decision-makers with the nuanced data needed to mitigate the impacts of floods and droughts in diverse climate regions.

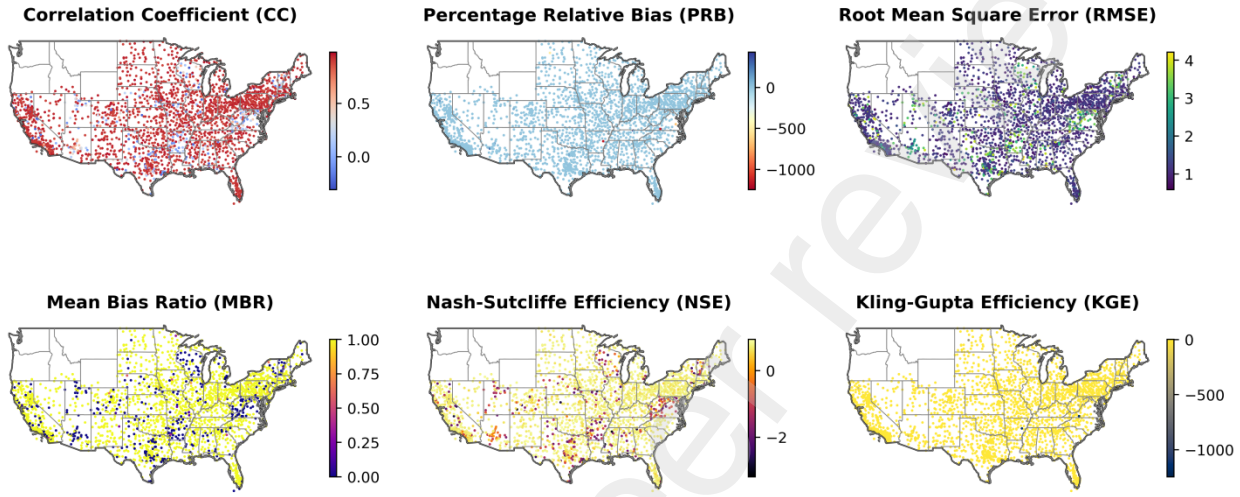

Figure 15. Spatial evaluation of the SRAI anomaly index across 2,360 stations in CONUS.

4.6 *Uncertainties in the proposed rainfall anomaly indices*

The two advanced indices used in this study (MRAI and SRAI) are not without uncertainties that may have been overlooked. The MRAI utilizes the minimum and maximum values from the AMS series, which ideally captures the full range of the AMS. However, a single outlier, if not properly managed, can skew the anomaly direction. To mitigate this issue, it is advisable to conduct a preliminary analysis of the AMS and remove any years identified as outliers or deemed necessary for exclusion.

On another note, SRAI employs the standard deviation instead of the mean. While the standard deviation is often considered a superior metric to the mean for computing anomalies, it

can present challenges when deviations are not extreme, potentially skewing the anomaly estimates in the direction of least deviation, typically toward positive values. Nevertheless, these uncertainties are relatively minimal compared to the traditional RAI index, which uses a crude approach by selecting the bottom ten values from the AMS to compute the RAI index. The RAI index has been reported to have less capacity to capture extremely dry and extremely wet anomalies (Raziei, 2021). In this regard, MRAI and SRAI effectively address this gap, as both indices demonstrate a greater ability to capture rainfall anomalies in extreme conditions, such as drought-prone and extremely wet environments.

Another uncertainty in this assessment arises from data disparity. RAI was modeled using NOAA station data, whereas both MRAI and SRAI were modeled from IMERG satellite precipitation data. The choice of IMERG was primarily to facilitate the scaling of the method beyond CONUS, as NOAA station data is limited to that region. IMERG offers global coverage and has been evaluated against NOAA station data in previous studies (K. Ekpetere, 2024; K. O. Ekpetere et al., 2024; K. O. Ekpetere & Coll, 2024), showing high agreement with station data. For localized studies, it is recommended that all three indices (MRAI, SRAI, and RAI) be subjected to the same data type, which has been identified as a future direction for this work.

5 Summary and Conclusion

This study provides a method advancement by proposing two rainfall anomaly indices – the MRAI and SRAI indices. The advance indices are intended to complement existing RAI index model, helping to capture extremely dry and extremely wet range of the rainfall anomaly spectrum. The developed indices were tested using IMERG data in CONUS and evaluated against the existing RAI index calculated from 2,360 NOAA station data as a reference. The

introduction of IMERG data were necessary to scale the model output beyond CONUS and cover data scarce locations. The PDF distribution of the models were assessed, and anomaly outputs evaluated temporarily and spatially, covering a wide range of locations in CONUS. The following observations were made:

1) The kurtosis value of MRAI lies between 0 and +0.9, while SRAI lies between -0.9 and -0.1. The median range RAI (reference) lies between -1 and +1, MRAI lies between 0 and +2, whereas SRAI lies between -2 and 0. Both Kurtosis and the median value range assessment show that MRAI leans towards extremely wet conditions and tends to detect extreme positive rainfall anomalies, whereas the SRAI leans towards extremely dry conditions and tends to detect extreme negative rainfall anomalies.

2) Comparing MRAI against RAI, the average CC were 0.946, PRB of -23.5, RMSE of 0.93, MBR of 0.74, NSE of 0.82, and KGE of 0.53. In contrast, comparing SRAI against RAI, average CC were 0.71, PRB of -14.5, RMSE of 1.7, MBR of 0.8, NSE of 0.41, and KGE of 0.46. MRAI showed capacity to detect extremely wet conditions in humid regions whereas SRAI showed tendency for dry areas.

3) Assessment across varying rainfall locations showed interesting results. In extremely wet locations (e.g., Louisiana), MRAI recorded the following average statistics – CC of 0.943, PRB of 0.075, RMSE of 0.923, MBR of 0.727, NSE of 0.815, and KGE of 0.036. The SRAI recorded average statistics of CC of 0.908, PRB of 1.38, RMSE of 1.21, MBR of 0.865, NSE of 0.678, and KGE of -1.330. Conversely, in dry locations (e.g., Nevada), the MRAI recorded following average statistics – CC of 0.957, PRB of 0.133, RMSE of 0.887, MBR of 0.819, NSE of 0.841, and KGE of 0.351. SRAI's

765 average statistics were CC of 0.582, PRB of -2.126, RMSE of 2.074, MBR of 0.557,
766 NSE of -0.119, and KGE of -3.84.

767
768 4) Spatially, the MRAI recorded CC values ranging from ≥ 0.90, PRB of approximately
769 0, RMSE between 0.5 and 1.25, MBR between 0.5 and 1, NSE between 0.7 and 0.9,
770 and KGE below 0. SRAI recorded an average CC between 0.30 and 0.90, PRB of
771 approximately 0 with a few outlier exceptions ≤ 0, RMSE between 1 and 4, MBR
772 between 0 and 1, NSE around 0, and KGE below 0. The pattern is consistent with (1).

773 The development of the MRAI and SRAI indices provides a refined toolset for monitoring
774 extreme rainfall anomalies across diverse climate regions, offering practical benefits to
775 policymakers and stakeholders in climate-sensitive fields. By effectively capturing both
776 extreme wet (MRAI) and dry (SRAI) anomalies, these indices address limitations in the
777 conventional RAI model, which has traditionally underrepresented the range of extreme rainfall
778 events. Through robust testing across 2,360 NOAA stations and validation with IMERG data,
779 this study confirms the indices' utility in regions like humid Louisiana and arid Nevada,
780 showcasing the MRAI's strength in wet conditions and SRAI's precision in dry climates. The
781 spatial and temporal insights gained from these indices allow for targeted monitoring, making
782 them valuable for water resource management, agricultural planning, urban infrastructure
783 resilience, and climate adaptation strategies. Policymakers can leverage these indices to better
784 prepare for flood and drought risks, allocate resources effectively, and develop tailored
785 strategies for climate adaptation based on specific regional climate profiles. The capacity to
786 scale these indices globally with IMERG data further extends their potential impact, providing
787 a versatile tool for addressing climate change and supporting sustainable development in diverse
788 and data-scarce regions worldwide. Future direction of this research will attempt further

validation of the advanced indices in regions outside of CONUS and provide a web application for calculating anomaly for locations globally.

Acknowledgements

This work was supported by the National Science Foundation under the Kansas NSF-EPSCoR, award number OIA-2148878.

Code and Data

Code and datasets: https://github.com/Kennethekpetere/Modified-Rainfall-Anomaly-Index

References

Adeel, Z., Bakkensen, L., Cabrera-Rivera, O., Franco, E., Garfin, G. M., McPherson, R. A., Méndez, K., & Wen, X. (2023). *Challenges in and Opportunities for International Collaboration: Costing Flood Damages and Losses across Canada, Mexico, and the United States*. https://doi.org/10.1175/BAMS-D-21-0141.1

Ahn, J., Cho, W., Kim, T., Shin, H., & Heo, J.-H. (2014). Flood Frequency Analysis for the Annual Peak Flows Simulated by an Event-Based Rainfall-Runoff Model in an Urban Drainage Basin. *Water*, *6*(12), Article 12. https://doi.org/10.3390/w6123841

Aksu, H., Taflan, G. Y., Yaldiz, S. G., & Akgül, M. A. (2023). Evaluation of IMERG for GPM satellite-based precipitation products for extreme precipitation indices over Turkiye. *Atmospheric Research*, *291*, 106826. https://doi.org/10.1016/j.atmosres.2023.106826

Alamri, N., & Subyani, A. (2017). Generation of Rainfall Intensity Duration Frequency (IDF) Curves for Ungauged Sites in Arid Region. *Earth Systems and Environment*, *1*, 8. https://doi.org/10.1007/s41748-017-0008-8

Anjum, M. N., Ding, Y., Shangguan, D., Ahmad, I., Ijaz, M. W., Farid, H. U., Yagoub, Y. E., Zaman, M., & Adnan, M. (2018). Performance evaluation of latest integrated multi-satellite retrievals for Global Precipitation Measurement (IMERG) over the northern highlands of Pakistan. *Atmospheric Research*, *205*, 134–146. https://doi.org/10.1016/j.atmosres.2018.02.010

814 Arias, P. A., Fu, R., & Mo, K. C. (2012). Decadal Variation of Rainfall Seasonality in the North American Monsoon
815 Region and Its Potential Causes. *Journal of Climate*, *25*(12), 4258–4274. https://doi.org/10.1175/JCLI-D-11-
816 00140.1
817 Armal, S., & Khanbilvardi, R. (2019). Anomalies in the US precipitation extremes and their association with different
818 modes of climate variability. *Hydrological Sciences Journal*, *64*(13), 1605–1615.
819 https://doi.org/10.1080/02626667.2019.1662026
820 Baratto, J., de Bodas Terassi, P. M., de Beserra de Lima, N. G., & Galvani, E. (2024). Precipitation Anomalies and
821 Trends Estimated via Satellite Rainfall Products in the Cananeia–Iguape Coastal System, Southeast Region of
822 Brazil. *Climate*, *12*(2), Article 2. https://doi.org/10.3390/cli12020022
823 Bathrellos, G. D., Karymbalis, E., Skilodimou, H. D., Gaki-Papanastassiou, K., & Baltas, E. A. (2016). Urban flood
824 hazard assessment in the basin of Athens Metropolitan city, Greece. *Environmental Earth Sciences*, *75*(4), 319.
825 https://doi.org/10.1007/s12665-015-5157-1
826 Bedane, H. R., Beketie, K. T., Fantahun, E. E., Feyisa, G. L., & Anose, F. A. (2022). The impact of rainfall variability
827 and crop production on vertisols in the central highlands of Ethiopia. *Environmental Systems Research*, *11*(1),
828 26. https://doi.org/10.1186/s40068-022-00275-3
829 Bonnin, Martin, Lin, Parzybok, Yekta, & Riley. (2006). *Precipitation-Frequency Atlas of the United States*.
830 Bono, R., Arnau, J., Alarcón, R., & Blanca, M. J. (2020). Bias, Precision, and Accuracy of Skewness and Kurtosis
831 Estimators for Frequently Used Continuous Distributions. *Symmetry*, *12*(1), Article 1.
832 https://doi.org/10.3390/sym12010019
833 Boota, M. W., Nabi, G., Abbas, T., Yaseen, M., Faisal, M., & Azam, M. I. (2015). *ESTIMATION OF PROBABLE*
834 *MAXIMUM FLOOD (PMF): A CASE STUDY OF POTHWAR REGION, PAKISTAN.* 5.
835 Brown, V. M., Keim, B. D., Kappel, W. D., Hultstrand, D. M., Peyrefitte, A. G., Black, A. W., Steinhilber, K. M., &
836 Muhlestein, G. A. (2020). *How Rare Was the August 2016 South-Central Louisiana Heavy Rainfall Event?*
837 https://doi.org/10.1175/JHM-D-19-0225.1
838 Byrne, S. M., Merrifield, M. A., Carter, M. L., Cayan, D. R., Flick, R. E., Gershunov, A., & Giddings, S. N. (2023).
839 Southern California winter precipitation variability reflected in 100-year ocean salinity record.
840 *Communications Earth & Environment*, *4*(1), 1–9. https://doi.org/10.1038/s43247-023-00803-8

841 Chen, H., Wu, Y.-C., Cheng, C.-C., & Teng, C.-Y. (2023). Effect of climate change-induced water-deficit stress on
842 long-term rice yield. *PLOS ONE*, *18*(4), e0284290. https://doi.org/10.1371/journal.pone.0284290
843 Chen, J., Liao, J., Lou, Y., Ma, S., Shen, G., & Zhang, L. (2022). High-resolution datasets for lake level changes in the
844 Qinghai-Tibetan Plateau from 2002 to 2021 using multi-altimeter data. *Earth System Science Data*
845 *Discussions*, 1–18. https://doi.org/10.5194/essd-2022-313
846 Córdova, M., Célleri, R., & van Delden, A. (2022). Dynamics of Precipitation Anomalies in Tropical South America.
847 *Atmosphere*, *13*(6), Article 6. https://doi.org/10.3390/atmos13060972
848 Corringham, T. W., McCarthy, J., Shulgina, T., Gershunov, A., Cayan, D. R., & Ralph, F. M. (2022). Climate change
849 contributions to future atmospheric river flood damages in the western United States. *Scientific Reports*, *12*(1),
850 13747. https://doi.org/10.1038/s41598-022-15474-2
851 Costa, J., & Rodrigues, G. (2017). Space-Time Distribution of Rainfall Anomaly Index (RAI) for the Salgado Basin,
852 Ceará State—Brazil. *Ciência e Natura*, *39*, 627. https://doi.org/10.5902/2179460X26080
853 Da Silva, N. A., Webber, B. G. M., Matthews, A. J., Feist, M. M., Stein, T. H. M., Holloway, C. E., & Abdullah, M. F.
854 A. B. (2021). Validation of GPM IMERG Extreme Precipitation in the Maritime Continent by Station and
855 Radar Data. *Earth and Space Science*, *8*(7), e2021EA001738. https://doi.org/10.1029/2021EA001738
856 De Paola, F., Giugni, M., Topa, M. E., & Bucchignani, E. (2014). Intensity-Duration-Frequency (IDF) rainfall curves,
857 for data series and climate projection in African cities. *SpringerPlus*, *3*(1), 133. https://doi.org/10.1186/2193-
858 1801-3-133
859 Dehaghani, A. M., Gohari, A., Zareian, M. J., & Torabi Haghighi, A. (2023). A comprehensive evaluation of the
860 satellite precipitation products across Iran. *Journal of Hydrology: Regional Studies*, *46*, 101360.
861 https://doi.org/10.1016/j.ejrh.2023.101360
862 Dekai Lu & Bin Yong. (2018). Evaluation and Hydrological Utility of the Latest GPM IMERG V5 and GSMaP V7
863 Precipitation Products over the Tibetan Plateau. *Remote Sensing*, *10*(12), 2022.
864 https://doi.org/10.3390/rs10122022
865 Devitt, L., Neal, J., Wagener, T., & Coxon, G. (2021). Uncertainty in the extreme flood magnitude estimates of large-
866 scale flood hazard models. *Environmental Research Letters*, *16*(6), 064013. https://doi.org/10.1088/1748-
867 9326/abfac4

868 Duque-Gardeazabal, N., & Rodríguez, E. A. (2023). Improving Rainfall Fields in Data-Scarce Basins: Influence of the
869 Kernel Bandwidth Value of Merging on Hydrometeorological Modeling. *Journal of Hydrologic Engineering*,
870 *28*(7), 04023017. https://doi.org/10.1061/JHYEFF.HEENG-5541
871 Ekpetere, K. (2024). *Assessment of the PMPs and Design Storms Estimated from the IMERG Satellite Precipitation*
872 *Data* [Ph.D., University of Kansas].
873 https://www.proquest.com/docview/3069356596/abstract/8C40F546AC214F51PQ/1
874 Ekpetere, K., Abdelkader, M., Ishaya, S., Makwe, E., & Ekpetere, P. (2023). Integrating Satellite Imagery and Ground-
875 Based Measurements with a Machine Learning Model for Monitoring Lake Dynamics over a Semi-Arid
876 Region. *Hydrology*, *10*(4), Article 4. https://doi.org/10.3390/hydrology10040078
877 Ekpetere, K., Li, X., & Frame, J. (2022). *Metadata for the Rapid Forcing Retrieval (RFR) Web Tool* [Dataset].
878 https://doi.org/10.4211/hs.60e32ac396044582b0ef9f976d3e4a29
879 Ekpetere, K. O., & Coll, J. M. (2024). *A Hybrid Probability Model for Extreme Precipitation Event Analysis:*
880 *Application to Imerg-Gpm and Validation Against Atlas-14 in Conus* (SSRN Scholarly Paper 4948328). Social
881 Science Research Network. https://doi.org/10.2139/ssrn.4948328
882 Ekpetere, K. O., Mehta, A. V., Coll, J. M., Liang, C., Onochie, S. O., & Ekpetere, M. C. (2024). *Extreme Rainfall*
883 *Anomalies Based on IMERG Remote Sensing Data in CONUS: A Multi-Decade Case Study via the IPE Web*
884 *Application* (2024091774). Preprints. https://doi.org/10.20944/preprints202409.1774.v1
885 Fadhel, S., Rico-Ramirez, M. A., & Han, D. (2017). Uncertainty of Intensity–Duration–Frequency (IDF) curves due to
886 varied climate baseline periods. *Journal of Hydrology*, *547*, 600–612.
887 https://doi.org/10.1016/j.jhydrol.2017.02.013
888 Faiers, G. E., Grymes, J. M., Keim, B. D., & Muller, R. A. (1994). A reexamination of extreme 24-hour rainfall in
889 Louisiana, USA. *Climate Research*, *4*(1), 25–31. https://www.jstor.org/stable/24863384
890 Fashae, O., Jolaade, O., & OLUSOLA, A. (2017). An Assessment of Digital Elevation Model for Geospatial Studies: A
891 Case Study of Alawa Town, Niger State, Nigeria. *Ife Research Publications in Geography*, *15*, 31–51.
892 Felder, G., Paquet, E., Penot, D., Zischg, A., & Weingartner, R. (2019). Consistency of Extreme Flood Estimation
893 Approaches. *Journal of Hydrologic Engineering*, *24*(7), 04019018. https://doi.org/10.1061/(ASCE)HE.1943-
894 5584.0001797

895 Gabriels, K., Willems, P., & Van Orshoven, J. (2022). A comparative flood damage and risk impact assessment of land
896 use changes. *Natural Hazards and Earth System Sciences*, *22*(2), 395–410. https://doi.org/10.5194/nhess-22-
897 395-2022
898 Gao, P., Carbone, G. J., Lu, J., & Guo, D. (2018). An Area-Based Approach for Estimating Extreme Precipitation
899 Probability. *Geographical Analysis*, *50*(3), 314–333. https://doi.org/10.1111/gean.12148
900 Gavahi, K., Abbaszadeh, P., & Moradkhani, H. (2022). How does precipitation data influence the land surface data
901 assimilation for drought monitoring? *Science of The Total Environment*, *831*, 154916.
902 https://doi.org/10.1016/j.scitotenv.2022.154916
903 Gebregiorgis, A. S., Kirstetter, P.-E., Hong, Y. E., Gourley, J. J., Huffman, G. J., Petersen, W. A., Xue, X., &
904 Schwaller, M. R. (2018). To What Extent is the Day 1 GPM IMERG Satellite Precipitation Estimate Improved
905 as Compared to TRMM TMPA-RT? *Journal of Geophysical Research: Atmospheres*, *123*(3), 1694–1707.
906 https://doi.org/10.1002/2017JD027606
907 Gershunov, A., Shulgina, T., Clemesha, R. E. S., Guirguis, K., Pierce, D. W., Dettinger, M. D., Lavers, D. A., Cayan,
908 D. R., Polade, S. D., Kalansky, J., & Ralph, F. M. (2019). Precipitation regime change in Western North
909 America: The role of Atmospheric Rivers. *Scientific Reports*, *9*(1), 9944. https://doi.org/10.1038/s41598-019-
910 46169-w
911 Gil-Alana, L. A., Gupta, R., Sauci, L., & Carmona-González, N. (2022). Temperature and precipitation in the US states:
912 Long memory, persistence, and time trend. *Theoretical and Applied Climatology*, *150*(3), 1731–1744.
913 https://doi.org/10.1007/s00704-022-04232-z
914 Gornall, J., Betts, R., Burke, E., Clark, R., Camp, J., Willett, K., & Wiltshire, A. (2010). Implications of climate change
915 for agricultural productivity in the early twenty-first century. *Philosophical Transactions of the Royal Society*
916 *B: Biological Sciences*, *365*(1554), 2973–2989. https://doi.org/10.1098/rstb.2010.0158
917 Gu, H., Ma, Z., & Li, M. (2016). Effect of a large and very shallow lake on local summer precipitation over the Lake
918 Taihu basin in China. *Journal of Geophysical Research: Atmospheres*, *121*(15), 8832–8848.
919 https://doi.org/10.1002/2015JD024098
920 Gu, L., Yin, J., Gentine, P., Wang, H.-M., Slater, L. J., Sullivan, S. C., Chen, J., Zscheischler, J., & Guo, S. (2023).
921 Large anomalies in future extreme precipitation sensitivity driven by atmospheric dynamics. *Nature*
922 *Communications*, *14*(1), 3197. https://doi.org/10.1038/s41467-023-39039-7

Henny, L., Thorncroft, C. D., & Bosart, L. F. (2023). *Changes in Seasonal Large-Scale Extreme Precipitation in the Mid-Atlantic and Northeast United States, 1979–2019*. https://doi.org/10.1175/JCLI-D-22-0088.1

Hoell, A., Quan, X.-W., Hoerling, M., Diaz, H. F., Fu, R., He, C., Lisonbee, J. R., Mankin, J. S., Seager, R., Sheffield, A., Simpson, I. R., & Wahl, E. R. (2022). *Water Year 2021 Compound Precipitation and Temperature Extremes in California and Nevada*. https://doi.org/10.1175/BAMS-D-22-0112.1

Hu, F., Zhang, L., Liu, Q., & Chyi, D. (2021). Environmental Factors Controlling the Precipitation in California. *Atmosphere*, *12*(8), Article 8. https://doi.org/10.3390/atmos12080997

Huang, H., Patricola, C. M., Winter, J. M., Osterberg, E. C., & Mankin, J. S. (2021). Rise in Northeast US extreme precipitation caused by Atlantic variability and climate change. *Weather and Climate Extremes*, *33*, 100351. https://doi.org/10.1016/j.wace.2021.100351

Huffman. (2020, January 3). *Algorithm Theoretical Basis Document (ATBD) Version 06 of NASA Global Precipitation Measurement (GPM) Integrated Multi-satellitE Retrievals for GPM (IMERG)*. NASA/GSFC Code 612. https://gpm.nasa.gov/sites/default/files/2020-05/IMERG_ATBD_V06.3.pdf

Huffman, Bolvin, D. T., Nelkin, E. J., Wolff, D. B., Adler, R. F., Gu, G., Hong, Y., Bowman, K. P., & Stocker, E. F. (2007). The TRMM Multisatellite Precipitation Analysis (TMPA): Quasi-Global, Multiyear, Combined-Sensor Precipitation Estimates at Fine Scales. *Journal of Hydrometeorology*, *8*(1), 38–55. https://doi.org/10.1175/JHM560.1

Iizumi, T., Iseki, K., Ikazaki, K., Sakai, T., Shiogama, H., Imada, Y., & Batieno, B. J. (2024). Increasing heavy rainfall events and associated excessive soil water threaten a protein-source legume in dry environments of West Africa. *Agricultural and Forest Meteorology*, *344*, 109783. https://doi.org/10.1016/j.agrformet.2023.109783

Kasi, V., Rathinasamy, M., & Jarajapu, D. (2022). Framework for developing IDF curves using satellite precipitation: A case study using GPM-IMERG V6 data. *Earth Science Informatics*, *15*, 1–17. https://doi.org/10.1007/s12145-021-00708-0

Kim, D.-E., Gourbesville, P., & Liong, S.-Y. (2019). Overcoming data scarcity in flood hazard assessment using remote sensing and artificial neural network. *Smart Water*, *4*(1), 2. https://doi.org/10.1186/s40713-018-0014-5

Kim, Y.-U., Webber, H., Adiku, S. G. K., Nóia Júnior, R. de S., Deswarte, J.-C., Asseng, S., & Ewert, F. (2024). Mechanisms and modelling approaches for excessive rainfall stress on cereals: Waterlogging, submergence,

lodging, pests and diseases. *Agricultural and Forest Meteorology*, *344*, 109819. https://doi.org/10.1016/j.agrformet.2023.109819

Klima, K. (2021, March 21). *Normality Testing—Skewness and Kurtosis | The GoodData Community*. https://community.gooddata.com/metrics-and-maql-kb-articles-43/normality-testing-skewness-and-kurtosis-241

Koudahe, K., Kayode, A. J., Samson, A. O., Adebola, A. A., & Djaman, K. (2017). Trend Analysis in Standardized Precipitation Index and Standardized Anomaly Index in the Context of Climate Change in Southern Togo. *Atmospheric and Climate Sciences*, *7*(4), Article 4. https://doi.org/10.4236/acs.2017.74030

Kumar, S., A. Ahmed, S., & Karkala, J. (2022). Evaluating the consistency of the TRMM over the rain gauge for drought monitoring in the semi-arid region of Karnataka, India, using statistical methods. *Environmental Science: Advances*, *1*(4), 517–529. https://doi.org/10.1039/D2VA00113F

LaRocque, A. (2013). Probable Maximum Flood (PMF). In P. T. Bobrowsky (Ed.), *Encyclopedia of Natural Hazards* (pp. 777–778). Springer Netherlands. https://doi.org/10.1007/978-1-4020-4399-4_276

Lau, A., & Behrangi, A. (2022). Understanding Intensity–Duration–Frequency (IDF) Curves Using IMERG Sub-Hourly Precipitation against Dense Gauge Networks. *Remote Sensing*, *14*, 5032. https://doi.org/10.3390/rs14195032

Le, P. V. V., Randerson, J. T., Willett, R., Wright, S., Smyth, P., Guilloteau, C., Mamalakis, A., & Foufoula-Georgiou, E. (2023). Climate-driven changes in the predictability of seasonal precipitation. *Nature Communications*, *14*(1), 3822. https://doi.org/10.1038/s41467-023-39463-9

Li, Y., Guan, K., Schnitkey, G. D., DeLucia, E., & Peng, B. (2019). Excessive rainfall leads to maize yield loss of a comparable magnitude to extreme drought in the United States. *Global Change Biology*, *25*(7), 2325–2337. https://doi.org/10.1111/gcb.14628

Mab, P., Ly, S., Chompuchan, C., & Kositsakulchai, E. (2019). *Evaluation of Satellite Precipitation from Google Earth Engine in Tonle Sap Basin, Cambodia*.

Mckee, T., Doesken, N., & Kleist, J. (1993). *The relationship of drought frequency and duration to time scales*. https://www.semanticscholar.org/paper/THE-RELATIONSHIP-OF-DROUGHT-FREQUENCY-AND-DURATION-Mckee-Doesken/c3f7136d6cb726b295eb34565a8270177c57f40f

McKitrick, R., & Christy, J. (2019). Assessing changes in US regional precipitation on multiple time scales. *Journal of Hydrology*, *578*, 124074. https://doi.org/10.1016/j.jhydrol.2019.124074

Min Yang, Zhongqin Li, Muhammad Naveed Anjum, & Yayu Gao. (2019). Performance Evaluation of Version 5 (V05) of Integrated Multi-Satellite Retrievals for Global Precipitation Measurement (IMERG) over the Tianshan Mountains of China. *Water*, *11*(6), 1139. https://doi.org/10.3390/w11061139

Mohammadi, S., Rydgren, K., Bakkestuen, V., & Gillespie, M. A. K. (2023). Impacts of recent climate change on crop yield can depend on local conditions in climatically diverse regions of Norway. *Scientific Reports*, *13*(1), 3633. https://doi.org/10.1038/s41598-023-30813-7

Nasta, P., Allocca, C., Deidda, R., & Romano, N. (2020). Assessing the impact of seasonal-rainfall anomalies on catchment-scale water balance components. *Hydrology and Earth System Sciences*, *24*(6), 3211–3227. https://doi.org/10.5194/hess-24-3211-2020

Ning, S., Song, F., Udmale, P., Jin, J., Thapa, B. R., & Ishidaira, H. (2017). Error Analysis and Evaluation of the Latest GSMap and IMERG Precipitation Products over Eastern China. *Advances in Meteorology*, *2017*, e1803492. https://doi.org/10.1155/2017/1803492

NOAA. (2017). *NOAA Atlas 14 Time Series Data of Annual Maximum Precipitation*. https://hdsc.nws.noaa.gov/hdsc/pfds/pfds_series.html

NOAA-OWP. (2022). *NOAA ATLAS 15: Update to the National Precipitation Frequency Standard*. NAA Office of Water Prediction. https://www.weather.gov/media/owp/hdsc_documents/NOAA_Atlas_15_Flyer.pdf

Noor, M., Ismail, T., Shahid, S., Asaduzzaman, M., & Dewan, A. (2021). Evaluating intensity-duration-frequency (IDF) curves of satellite-based precipitation datasets in Peninsular Malaysia. *Atmospheric Research*, *248*, 105203. https://doi.org/10.1016/j.atmosres.2020.105203

NWS, N. (2020). *HDSC PMP Documents*. NOAA's National Weather Service. https://www.weather.gov/owp/hdsc_pmp

Palmer, W. (2006). *Meteorological Drought. Research Paper No. 45, 1965, 58 p.* 1–65.

Pan, L.-L., Chen, S.-H., Cayan, D., Lin, M.-Y., Hart, Q., Zhang, M.-H., Liu, Y., & Wang, J. (2011). Influences of climate change on California and Nevada regions revealed by a high-resolution dynamical downscaling study. *Climate Dynamics*, *37*(9), 2005–2020. https://doi.org/10.1007/s00382-010-0961-5

1004 Peinó, E., Bech, J., & Udina, M. (2023). *Dependence of GPM IMERG products on precipitation intensity in Catalonia.*
1005 (EGU23-12109). EGU23. Copernicus Meetings. https://doi.org/10.5194/egusphere-egu23-12109
1006 Perica, S., Lin, B., Martin, D., Martin, F., Brewer, D., Trypaluk, C., Yekta, M., Hiner, L., Heim, S., Dietz, S., Parzybok,
1007 T., Chen, L.-C., Maitaria, K., Chen, R., Roy, I., Unruh, D., Zhao, T., Yarchoan, J., & Bonnin, G. (2011).
1008 *NOAA Atlas 14 Precipitation-Frequency Atlas of the United States*. *5*(3.0).
1009 https://www.weather.gov/media/owp/oh/hdsc/docs/Atlas14_Volume5.pdf
1010 Perica, S., Martin, D., Pavlovic, S., Roy, I., St. Laurent, M., Trypaluk, C., Unruh, D., Yekta, M., & Bonnin, G. (2013).
1011 *Precipitation-Frequency Atlas of the United States*.
1012 Pilgrim, D. H., & Cordery, I. (1975). Rainfall Temporal Patterns for Design Floods. Journal of the Hydraulics Division,
1013 101(1), 81–95. https://doi.org/10.1061/JYCEAJ.0004197
1014 Pradhan, R. K., Markonis, Y., Vargas Godoy, M. R., Villalba-Pradas, A., Andreadis, K. M., Nikolopoulos, E. I.,
1015 Papalexiou, S. M., Rahim, A., Tapiador, F. J., & Hanel, M. (2022). Review of GPM IMERG performance: A
1016 global perspective. *Remote Sensing of Environment*, *268*, 112754. https://doi.org/10.1016/j.rse.2021.112754
1017 Pucknell, S., Kjeldsen, T., Haxton, T., Jeans, J., & Young, A. (2020). Estimating the probable maximum flood in UK
1018 catchments using the ReFH model. *Dams and Reservoirs*, *30*(3), 85–90. https://doi.org/10.1680/jdare.20.00015
1019 Quinn, N., Bates, P. D., Neal, J., Smith, A., Wing, O., Sampson, C., Smith, J., & Heffernan, J. (2019). The Spatial
1020 Dependence of Flood Hazard and Risk in the United States. *Water Resources Research*, *55*(3), 1890–1911.
1021 https://doi.org/10.1029/2018WR024205
1022 Raziei, T. (2021). Revisiting the Rainfall Anomaly Index to serve as a Simplified Standardized Precipitation Index.
1023 *Journal of Hydrology*, *602*, 126761. https://doi.org/10.1016/j.jhydrol.2021.126761
1024 Ripple, W. J., Wolf, C., Gregg, J. W., Rockström, J., Mann, M. E., Oreskes, N., Lenton, T. M., Rahmstorf, S.,
1025 Newsome, T. M., Xu, C., Svenning, J.-C., Pereira, C. C., Law, B. E., & Crowther, T. W. (2024). The 2024
1026 state of the climate report: Perilous times on planet Earth. *BioScience*, biae087.
1027 https://doi.org/10.1093/biosci/biae087
1028 Sathianarayanan, M., & Hsu, P.-H. (2023). SPATIAL DOWNSCALING OF GPM IMERG V06 GRIDDED
1029 PRECIPITATION USING MACHINE LEARNING ALGORITHMS. *The International Archives of the*
1030 *Photogrammetry, Remote Sensing and Spatial Information Sciences*, *XLVIII-4/W6-2022*, 327–332.
1031 https://doi.org/10.5194/isprs-archives-XLVIII-4-W6-2022-327-2023

1032 Schamm, K., Ziese, M., Becker, A., Finger, P., Meyer-Christoffer, A., Schneider, U., Schröder, M., & Stender, P.
1033 (2014). Global gridded precipitation over land: A description of the new GPCC First Guess Daily product.
1034 *Earth System Science Data*, *6*(1), 49–60. https://doi.org/10.5194/essd-6-49-2014
1035 Seleiman, M. F., Al-Suhaibani, N., Ali, N., Akmal, M., Alotaibi, M., Refay, Y., Dindaroglu, T., Abdul-Wajid, H. H., &
1036 Battaglia, M. L. (2021). Drought Stress Impacts on Plants and Different Approaches to Alleviate Its Adverse
1037 Effects. *Plants*, *10*(2), 259. https://doi.org/10.3390/plants10020259
1038 Singh, J., Karmakar, S., PaiMazumder, D., Ghosh, S., & Niyogi, D. (2020). Urbanization alters rainfall extremes over
1039 the contiguous United States. *Environmental Research Letters*, *15*(7), 074033. https://doi.org/10.1088/1748-
1040 9326/ab8980
1041 Tan, M. L., & Santo, H. (2018). Comparison of GPM IMERG, TMPA 3B42 and PERSIANN-CDR satellite
1042 precipitation products over Malaysia. *Atmospheric Research*, *202*, 63–76.
1043 https://doi.org/10.1016/j.atmosres.2017.11.006
1044 Tan, M. L., & Yang, X. (2020). Effect of rainfall station density, distribution and missing values on SWAT outputs in
1045 tropical region. *Journal of Hydrology*, *584*, 124660. https://doi.org/10.1016/j.jhydrol.2020.124660
1046 Tang, S., Li, R., He, J., Wang, H., Fan, X., & Yao, S. (2020, February 1). *Comparative Evaluation of the GPM IMERG*
1047 *Early, Late, and Final Hourly Precipitation Products Using the CMPA Data over Sichuan Basin of China*.
1048 Water; MDPI AG. https://doi.org/10.3390/w12020554
1049 Tibbetts, J. (2006). Louisiana's Wetlands: A Lesson in Nature Appreciation. *Environmental Health Perspectives*,
1050 *114*(1), A40–A43. https://www.ncbi.nlm.nih.gov/pmc/articles/PMC1332684/
1051 Trinh, T., Diaz, A., Iseri, Y., Snider, E., Anderson, M. L., Carr, K. J., & Kavvas, M. L. (2022). A numerical coupled
1052 atmospheric–hydrologic modeling system for probable maximum flood estimation with application to
1053 California's southern Sierra Nevada foothills watersheds. *Journal of Flood Risk Management*, *n/a*(n/a),
1054 e12809. https://doi.org/10.1111/jfr3.12809
1055 Van-rooy, M. P. (1965). *A Rainfall Anomaly Index (RAI), Independent of the Time and Space.* [Graphic].
1056 https://www.scirp.org/reference/referencespapers?referenceid=3722343
1057 VDCR. (2015). *Probable Maximum Precipitation Study and Evaluation Tool (Virginia Department of Conservation*
1058 *and Recreation)*. Virginia Department of Conservation and Recreation. https://www.dcr.virginia.gov/dam-
1059 safety-and-floodplains/pmp-tool

Vicente-Serrano, S. M., Beguería, S., & López-Moreno, J. I. (2010). *A Multiscalar Drought Index Sensitive to Global Warming: The Standardized Precipitation Evapotranspiration Index*. https://doi.org/10.1175/2009JCLI2909.1

Viglione, A., & Blöschl, G. (2009). On the role of storm duration in the mapping of rainfall to flood return periods. Hydrology and Earth System Sciences, 13(2), 205–216. https://doi.org/10.5194/hess-13-205-2009

Wang, J., Petersen, W. A., & Wolff, D. B. (2021). Validation of Satellite-Based Precipitation Products from TRMM to GPM. *Remote Sensing*, *13*(9), 1745. https://doi.org/10.3390/rs13091745

Wang, S., Zuo, H., Yin, Y., Hu, C., Yin, J., Ma, X., & Wang, J. (2019). Interpreting Rainfall Anomalies Using Rainfall's Nonnegative Nature. *Geophysical Research Letters*, *46*(1), 426–434. https://doi.org/10.1029/2018GL081190

Wang, Y., Miao, C., Zhao, X., Zhang, Q., & Su, J. (2023). Evaluation of the GPM IMERG product at the hourly timescale over China. *Atmospheric Research*, *285*, 106656. https://doi.org/10.1016/j.atmosres.2023.106656

Wasko, C., Guo, D., Ho, M., Nathan, R., & Vogel, E. (2023). Diverging projections for flood and rainfall frequency curves. Journal of Hydrology, 620, 129403. https://doi.org/10.1016/j.jhydrol.2023.129403

Weng, P., Tian, Y., Jiang, Y., Chen, D., & Kang, J. (2023). Assessment of GPM IMERG and GSMaP daily precipitation products and their utility in droughts and floods monitoring across Xijiang River Basin. *Atmospheric Research*, *286*, 106673. https://doi.org/10.1016/j.atmosres.2023.106673

Willems, P. (1999). Stochastic generation of spatial rainfall for urban drainage areas. *Water Science and Technology*, *39*(9), 23–30. https://doi.org/10.1016/S0273-1223(99)00212-7

Willems, P. (2000). Compound intensity/duration/frequency-relationships of extreme precipitation for two seasons and two storm types. *Journal of Hydrology*, *233*(1), 189–205. https://doi.org/10.1016/S0022-1694(00)00233-X

Wilson, A. B., Avila-Diaz, A., Oliveira, L. F., Zuluaga, C. F., & Mark, B. (2022). Climate extremes and their impacts on agriculture across the Eastern Corn Belt Region of the U.S. *Weather and Climate Extremes*, *37*, 100467. https://doi.org/10.1016/j.wace.2022.100467

WMO. (2009). *Manual on estimation of probable maximum precipitation (PMP)*. https://googledrive.com/host/0BwdvoC9AeWjUazhkNTdXRXUzOEU/wmo_1045_en.pdf

Xin, Y., Yang, Y., Chen, X., Yue, X., Liu, Y., & Yin, C. (2022). Evaluation of IMERG and ERA5 precipitation products over the Mongolian Plateau. *Scientific Reports*, *12*(1), Article 1. https://doi.org/10.1038/s41598-022-26047-8

Xu, Y., Zhao, Y., Wu, Y., & Gao, C. (2022). Change patterns of precipitation anomalies and possible teleconnections with large-scale climate oscillations over the Yangtze River Delta, China. *Journal of Water and Climate Change*, *13*(8), 2972–2990. https://doi.org/10.2166/wcc.2022.097

Yu, L., Zhong, S., Pei, L., Bian, X., & Heilman, W. E. (2016). Contribution of large-scale circulation anomalies to changes in extreme precipitation frequency in the United States. *Environmental Research Letters*, *11*(4), 044003. https://doi.org/10.1088/1748-9326/11/4/044003

Yu, Z., Jiang, P., Gautam, M. R., Zhang, Y., & Acharya, K. (2015). Changes of seasonal storm properties in California and Nevada from an ensemble of climate projections. *Journal of Geophysical Research: Atmospheres*, *120*(7), 2676–2688. https://doi.org/10.1002/2014JD022414

Yuan, F., Wang, B., Shi, C., Cui, W., Zhao, C., Liu, Y., Ren, L., Zhang, L., Zhu, Y., Chen, T., Jiang, S., & Yang, X. (2018). Evaluation of hydrological utility of IMERG Final run V05 and TMPA 3B42V7 satellite precipitation products in the Yellow River source region, China. *Journal of Hydrology*, *567*, 696–711. https://doi.org/10.1016/j.jhydrol.2018.06.045

Yuan, F., Zhang, L., Ren, L., Zhao, C., Zhu, Y., Jiang, S., & Liu, Y. (2019). Applications of TRMM- and GPM-Era Multiple-Satellite Precipitation Products for Flood Simulations at Sub-Daily Scales in a Sparsely Gauged Watershed in Myanmar. *Remote Sensing*, *11*(2). https://doi.org/10.3390/rs11020140

Zachariah, M., Mondal, A., Das, M., AchutaRao, K. M., & Ghosh, S. (2020). On the role of rainfall deficits and cropping choices in loss of agricultural yield in Marathwada, India. *Environmental Research Letters*, *15*(9), 094029. https://doi.org/10.1088/1748-9326/ab93fc

Zaveri, E., Russ, J., & Damania, R. (2020). Rainfall anomalies are a significant driver of cropland expansion. Proceedings of the National Academy of Sciences, 117(19), 10225–10233. https://doi.org/10.1073/pnas.1910719117

Zhang, G., Su, X., Singh, V. P., & Ayantobo, O. O. (2021). Appraising standardized moisture anomaly index (SZI) in drought projection across China under CMIP6 forcing scenarios. *Journal of Hydrology: Regional Studies*, *37*, 100898. https://doi.org/10.1016/j.ejrh.2021.100898

Zhang, Y., Li, R., & Wang, K. (2023). Climatology and changes in internal intensity distributions of global precipitation systems over 2001–2020 based on IMERG. *Journal of Hydrology*, *620*, 129386. https://doi.org/10.1016/j.jhydrol.2023.129386

1116 Zhao, G., Li, Y., Zhou, L., & Gao, H. (2022). Evaporative water loss of 1.42 million global lakes. *Nature*
1117 *Communications*, *13*(1), Article 1. https://doi.org/10.1038/s41467-022-31125-6
1118 Zhao, H., Yang, B., Yang, S., Huang, Y., Dong, G., Bai, J., & Wang, Z. (2018). Systematical estimation of GPM-based
1119 global satellite mapping of precipitation products over China. *Atmospheric Research*, *201*, 206–217.
1120 https://doi.org/10.1016/j.atmosres.2017.11.005
1121 Zhou, Z., Lu, D., Yong, B., Shen, Z., Wu, H., & Yu, L. (2023). Evaluation of GPM-IMERG Precipitation Product at
1122 Multiple Spatial and Sub-Daily Temporal Scales over Mainland China. *Remote Sensing*, *15*(5), Article 5.
1123 https://doi.org/10.3390/rs15051237
1124 Zischg, A. P., Felder, G., Weingartner, R., Quinn, N., Coxon, G., Neal, J., Freer, J., & Bates, P. (2018). Effects of
1125 variability in probable maximum precipitation patterns on flood losses. *Hydrology and Earth System Sciences*,
1126 *22*(5), 2759–2773. https://doi.org/10.5194/hess-22-2759-2018
1127